PROCEEDINGS OF SCIENCE

Accelerator Physics for ILC and CLIC

Frank Zimmermann[1]
CERN, BE Department
Route de Meyrin, 1211 Geneva 23, Switzerland
E-mail: frank.zimmermann@cern.ch

This paper summarizes the second part of the "accelerator physics lectures" delivered at the Ambleside Linear Collider School 2009. It discusses more specific linear-collider issues: superconducting and room-temperature linear accelerators, particle sources for electrons and positrons, synchrotron radiation and damping, intensity limits, beam stability, and beam delivery system – including final focus, collimation, and beam-beam effects. It also presents an overview of the International Linear Collider (ILC), a description of the two beam acceleration scheme of the Compact Linear Collider (CLIC), and a comparison of the ILC and CLIC parameters.

Third Linear Collider Physics School 2009 – LCPS2009
Ambleside, UK
August 17-23, 2009

[1] Speaker

PoS(LCPS2009)007

1. Introduction

This paper summarizes the second part of the "accelerator physics lectures" delivered at the Ambleside Linear Collider School 2009. While the first part by E. Wilson covered accelerator fundamentals – synchrotrons, storage rings, linacs, Hill's equation and transverse focusing, phase stability, beam emittance and emittance conservation, luminosity, nonlinear effects, and the collision region –, this second part looks at more specific linear-collider issues: superconducting and room-temperature linear accelerators, particle sources for electrons and positrons, synchrotron radiation and damping, intensity limits, beam stability, and beam delivery system – including final focus, collimation, and beam-beam effects. The paper concludes with an overview of the International Linear Collider (ILC), a description of the two beam acceleration scheme of the Compact Linear Collider (CLIC), and a comparison of the ILC and CLIC parameters.

2. Superconducting and Room-Temperature Linacs

We here sketch the basics of radio-frequency (RF) acceleration, looking at Floquet theory and dispersion relations for accelerating structures; at cavity resonators; at RF microwave linacs: CLIC and ILC; at the luminosity challenges: gradient and efficiency; at superconducting (SC) cavities: cavity preparation, RF superconductivity, and performance; at structure optimization for normal-conducting (NC) cavities; and at RF power sources.

2.1 Radiofrequency Acceleration

The most common technique to accelerate charged particles to high energies is by means of a *radiofrequency (RF)* field. At a fixed location such RF field is seen to periodically vary in time, as illustrated in Fig. 1 (top). The beams to be accelerated are concentrated in so-called "*bunches*", typically comprising 10^9-10^{10} individual particles. For efficient acceleration, the bunch length must be short compared with the RF oscillation period and the bunches should be located close to the peak of the longitudinal electric field. Figure 1 (bottom) shows a schematic snapshot of the spatial field shape & bunch distribution taken at a fixed moment in time. The spatial field shape need not be sinusoidal (in this example it is rectangular), but again the accelerating bunches are found in the regions where the electric field is maximum. The goal of the accelerator designer is to ensure the synchronization between the radiofrequency field and the charged particles in such a way that the latter remain in the region of high electric field, both in time and in space, until they reach the end of both the single "accelerating structure" and of the full linear accelerator.

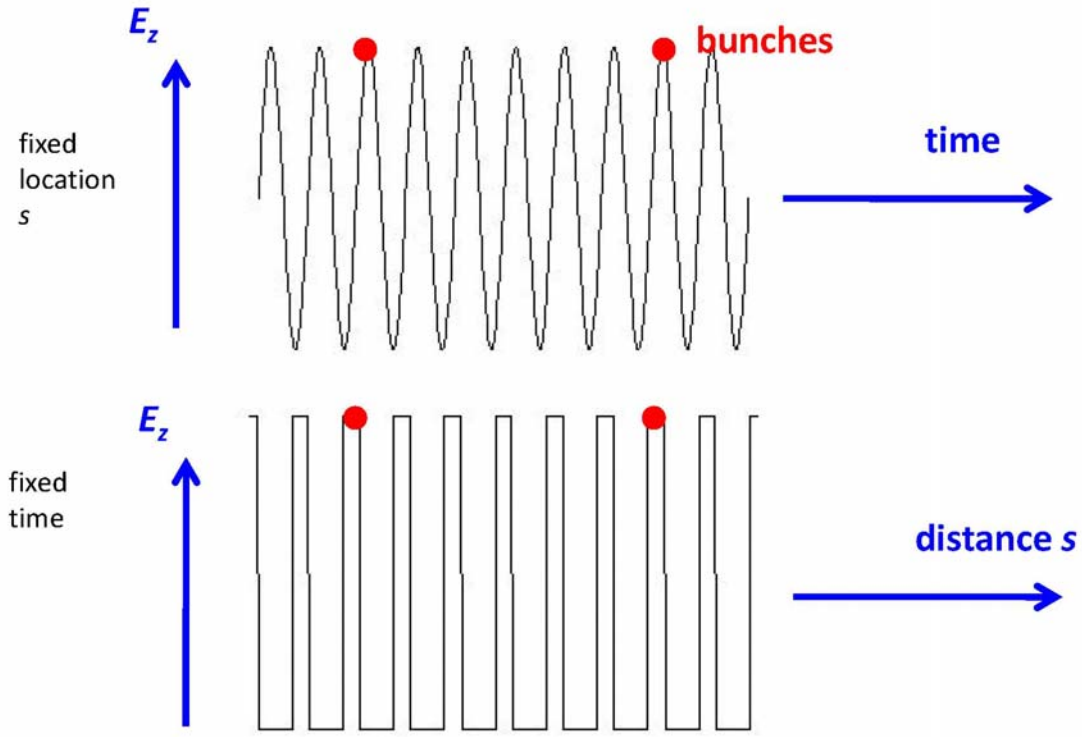

Figure 1: Schematic of radiofrequency acceleration with synchronism between the charged particle bunches and an electromagnetic wave. Top: time variation at a fixed location; bottom: snapshot at a fixed time.

More formally, an RF accelerating structure is a converter of RF power into (longitudinal) electric field and hence into electron energy [1]. Efficient acceleration is achieved if the electric field is concentrated in space and time, and if there is a synchronism of the electromagnetic wave with the charged particles. In a uniform waveguide the phase velocity of the electromagnetic wave, v_{ph} , approaches the light velocity asymptotically for high RF frequencies. The simplest and straigthforward method to reduce the phase velocity is the use of disc-loaded structures with individual cells coupled through the beam holes. Figure 2 illustrates that the disk-loaded waveguide and a chain of coupled cavities represent a transition between a set of individual cavities and a waveguide. A linear accelerator, or short "linac", consists of many accelerating structures of the type shown in Fig. 2. Of course the field in individual structures must be synchronized so that the particle bunches remain close to the crest of the RF wave as they travel from one structure to the next.

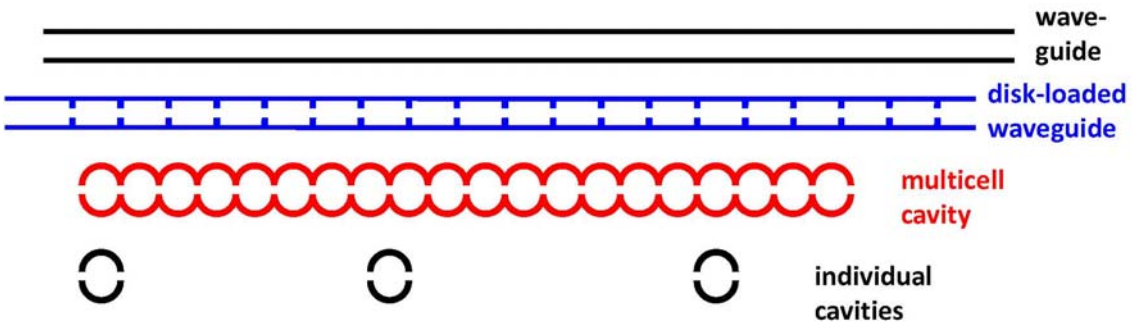

Figure 2: A disk-loaded waveguide is equivalent to a chain of coupled cavities. Extreme limiting cases on either side are the uniform waveguide and isolated cavities, respectively.

2.2 Floquet Theory and Dispersion Relation

The dispersion relation, i.e. the relation between frequency and wave number, can be understood, and reconstructed, by starting from either of the two extreme cases (that is from single cavities or from a uniform waveguide) and then applying a perturbative treatment. The result exhibits properties of both. In particular, a disk-loaded wave guide behaves similarly to a chain of coupled cavities. A "Brillouin" dispersion diagram for a disk-loaded waveguide is shown in Fig. 3. For efficient acceleration of ultrarelativistic particles the phase velocity should be (nearly) equal to the speed of light, which is the case at the points of intersection of the dispersion curve with the straight line representing propagation at the speed of light. The figure also shows that for a uniform (unloaded) waveguide the phase velocity always exceeds the speed of light and no efficient energy transfer or acceleration is possible.

A general electromagnetic wave in a periodic structrue can be described by Floquet theory (its 3D equivalent in solid-state physics is known as the Bloch theorem), according to which the following decomposition is always possible:

$$E_z = \sum_{n=-\infty}^{n=\infty} a_n \, J_0(k_{rn}\, r)\;\; e^{\,i(\omega t - k_n z)}$$

$$\text{where } k_n = k_0 + 2\pi n / L \;\text{ and }\quad k_{rn}^2 = \left(\frac{\omega}{c}\right)^2 - k_n^2$$

with $k_0=\omega/c$, and the k_n for $n>0$ being referred to as *space harmonics*. The waves corresponding to the space harmonics are far from synchronized with the beam and do not conribute to the acceleration. The above formulae show that (1) in the limit $v\rightarrow c$ the synchronous wave number vanishes, $k_{r0}=0$, and the accelerating force becomes independent of the radial position of the synchronous particle. From the equivalent formulae for the transverse force one can also show that (2) the radial force is proportional to the radial position and acting defocusing, and that it disappears as the particle velocity approaches the velocity of light. The two properties (1) and (2) greatly facilitate the operation of electron linacs.

Figure 4 presents an extended Brillouin diagram including several space harmonics, and on the right side, it shows snapshots of field patterns for different value of kL.

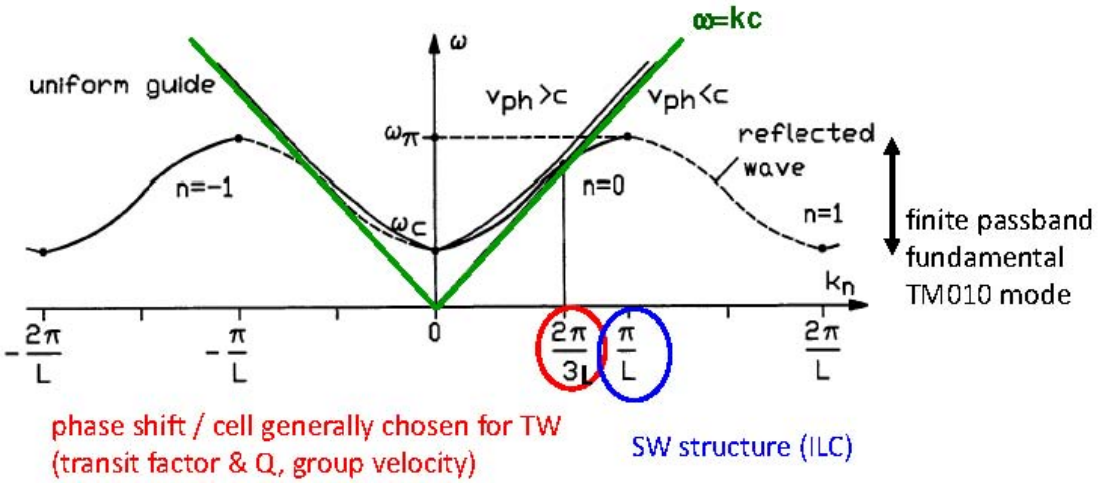

Figure 3: Brillouin dispersion diagram of a disk-loaded waveguide compared with a uniform waveguide [1]. A typical wavenumber used in operation for normal-conducting traveling wave structures is $2\pi/(3L)$ – chosen as a compromise between "transit factor", quality factor and group velocity – w ith L denoting the period length of the structure (that is the spacing between disks or cavity cells). For superconducting standing wave structures a typical k_0 value is π/L, as indicated.

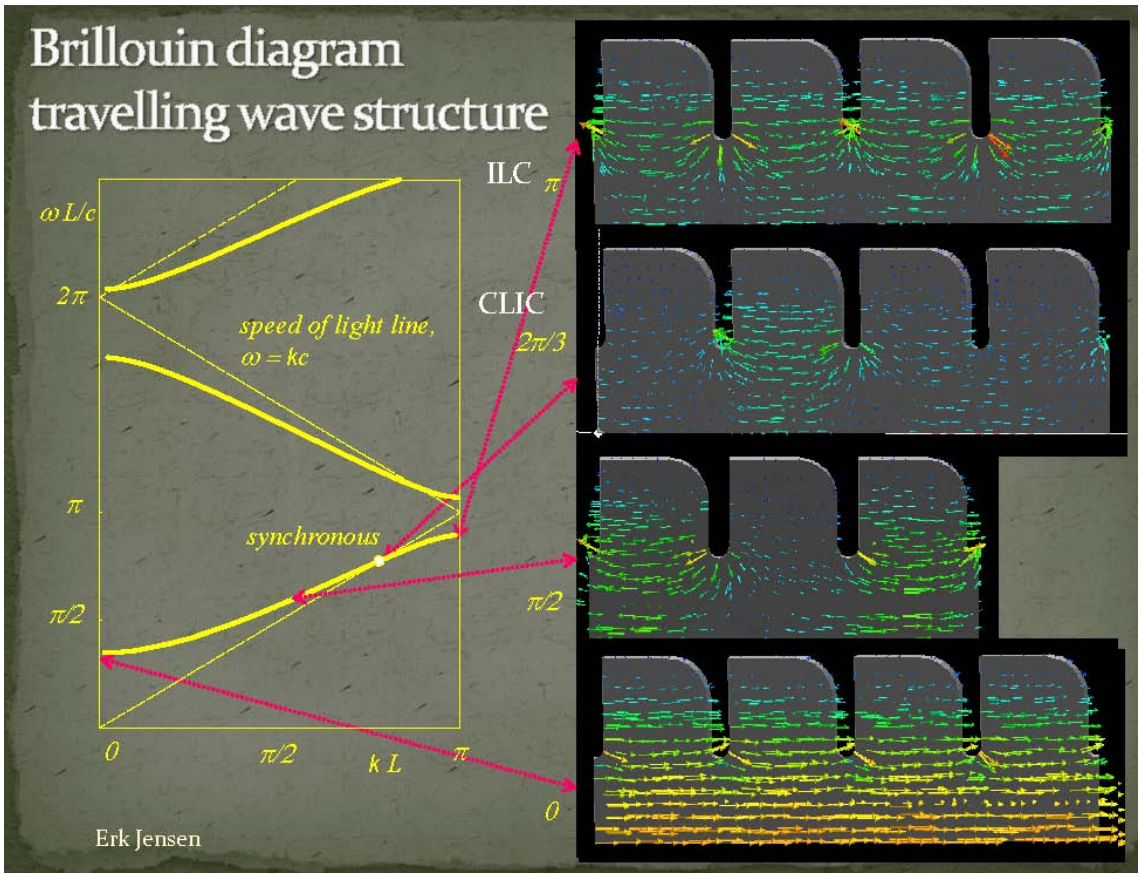

Figure 4: Brillouin diagram for travelling wave structure and snapshots of the electrical field pattern for different values of kL [2].

2.3 Cavity Resonators

When using RF fields in cavity resonators the accelerating voltage can be written as [3]

$$U = \sqrt{R/Q * \omega * W}$$

where W denotes the stored RF energy, which itself can be expressed as $W=Q\,P\,/\,\omega$, with P the RF power and Q the quality factor of the cavity. A very high Q value means that a very small RF power suffices to build up a high voltage. Only the power extracted by the beam needs to be replaced. For superconducting cavities the typical Q value is of order 10^{10}, for copper cavities about 10^4. The effect of the Q value on the cavity resonance impedance is illustrated in Fig. 5.

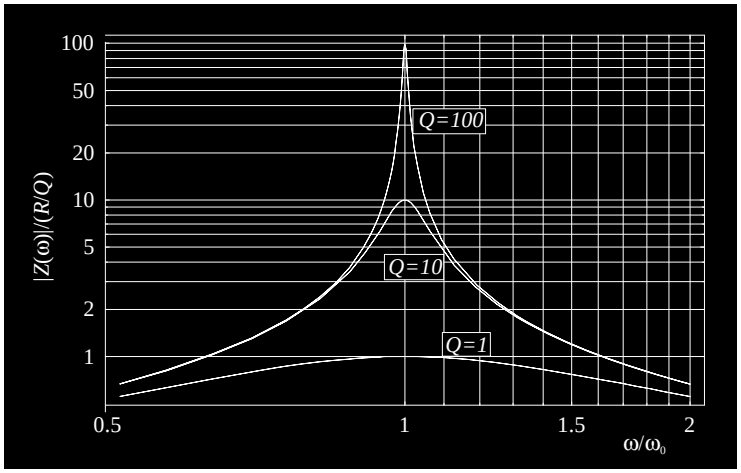

Figure 5: Cavity resonance impedance for different values of the quality factor Q [2].

2.4 RF Microwave Linacs: CLIC and ILC

The RF acceleration is THE technology which could provide TeV range e+/e- collisions in the near future [4]. Two examples for RF microwave acceleration are:

- "L-band" (1.3 GHz, or 20 cm). superconducting cavity, standing wave (ILC)
- "X-band" (11-12 GHz, ~2.6 cm), normal conducting cavity, traveling wave (CLIC)

The band names date back to the Second World War.

Figure 6 presents a photo of a CLIC normal-conducting RF accelerating structure made from copper, and the schematic of a single half cell [3]. The cell iris radius varies between about 2.35 and 3.3 mm. The CLIC X-band structure consists of 18 (or 20) cells, with a cell length of about 1 cm, providing an acceleration by about 20 MV over 20 cm. The CLIC collider will contain about 140,000 20-cell NC cavities, each one about 20 cm long.

The ILC RF structure is made from superconducting (SC) niobium and operates at 1.3 GHz. Consequently all cavity dimensions are about 10 times larger than for CLIC. A 9-cell SC L-band structure with a cell length of 10 cm achieves about 30 MV accelerating voltage over 1 m [which is about 3 times lower than the CLIC accelerating gradient]. The ILC cell iris radius is about 35 mm. The ILC project features 16,000 9-cell SC cavities, each one about 1 m long. Figure 7 shows a photo and a schematic of the ILC accelerating structure [3].

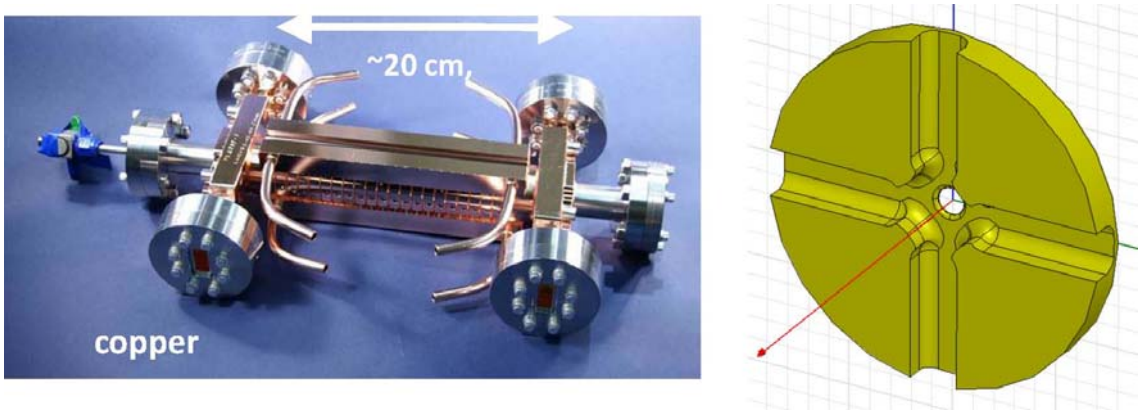

Figure 6: Photo of an 18-cell copper X-band structure for CLIC (left) and schematic of a structure half cell (right) [3,5].

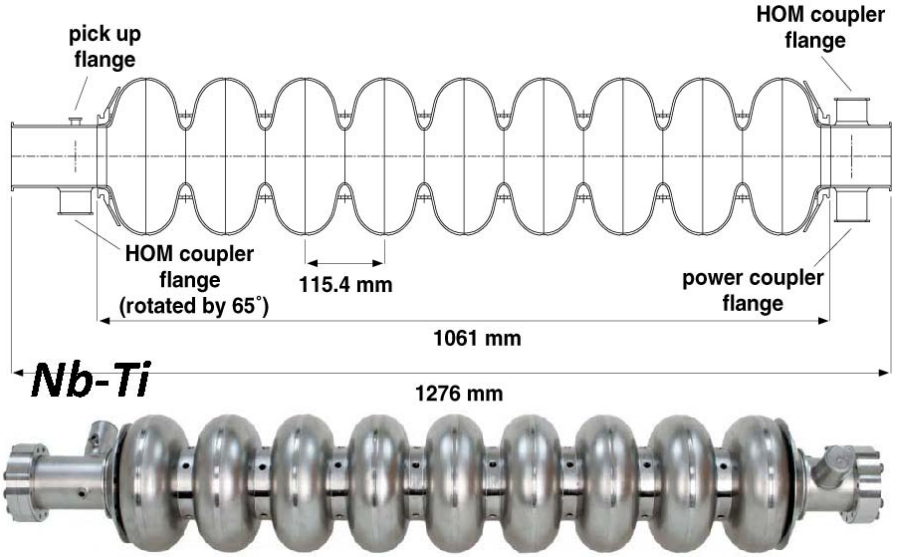

Figure 7: Schematic (top) and photo (bottom) of a 9-cell niobium ILC accelerating structure [3].

The geometric optimization of accelerating structure aims for a *shunt impedance* as high as possible (to minimize the dissipated power for a given accelerating field) and for a *surface field* as low as possible (the surface field limits the maximum achievable accelerating field). The shunt impedance is defined as [1]

$$R = \frac{E_a^2}{dP/dz}$$

with E_a the effective accelerating field experienced by the particle and dP/dz the power dissipated per unit length. The maximum magnetic field is reached close to the cavity equator and the maximum electric field close to the iris. Either of these two surface fields can limit the maximum accelerating gradient. The value of R/Q is a geometric factor that depends on the shape of the cavity.

Table 1: Linac cavity parameters for ILC and CLIC [1].

	SC SW 1.3 GHz	NC TW 12 GHz
R/Q	~1 kΩ/m	~16 kΩ/m
Q	10^{10}	~6200
R	10^7 MΩ/m	100 MΩ/m
E_s/E_{acc} (peak surface field / accelerating field)	~2	idem
H_s/H_{acc} (peak surface field / accelerating field)	~4 mT/(MV/m)	idem

Normal-conducting standing wave structures would have high Ohmic losses. Therefore, normal-conducting linacs operate with *traveling wave (TW) structures*, where the RF energy 'flows' with group velocity v_G along the structure into a load at the structure exit, as illustrated in Fig. 8.

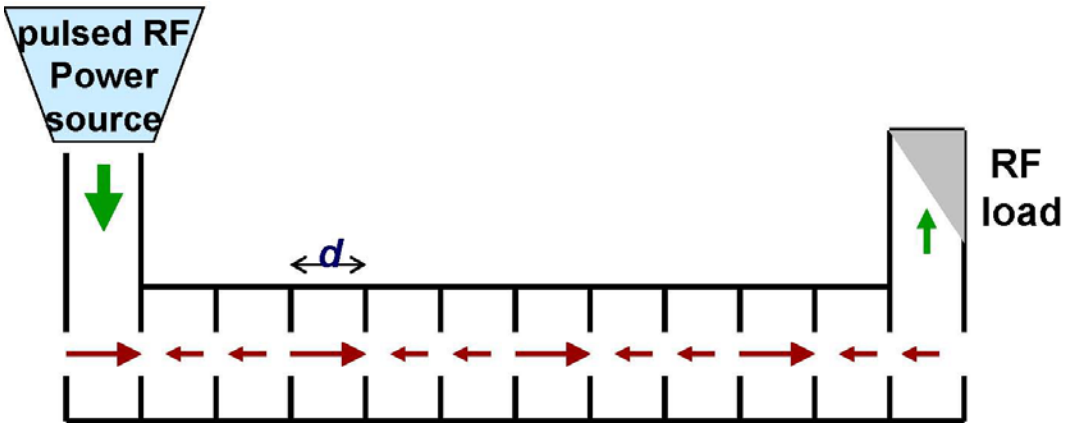

Figure 8: Schematic of a traveling-wave linac structure [5].

By contrast, superconducting cavities have small Ohmic losses and allow for *standing-wave (SW)* operation where the energy remains in the cavity over extended periods of time.

The shunt impedance for a traveling wave linac is twice that of a standing wave linac, i.e. $R/Q_{TW} = R/Q_{SW}$ x 2 [4]. The reason is that the space harmonics of the standing wave which is propagating against beam cannot contribute to the net acceleration, while the reverse-direction power is needed to establish the SW field. Many normal-conducting linacs at high gradient use traveling waves, since a high field needs high impedance. For TW acceleration, the power not used for beam acceleration and not lost in the wall needs to be absorbed by an outside RF load. The microwave power flows in one direction, and the beam is coupled to the field associated with this power flow.

A SC linac (at 2 K) needs cryo power to maintain the structure in the superconducting state. For a 1.3-GHz SC linac like ILC the heat load required can be expressed as the sum of a static and a dynamic term [6]

$$P_{cr} = A\frac{E}{g} + BDEg$$

where g designates the accelerating gradient in eV/m, E the total beam energy gain through the linac, and - extracted from the ILC and XFEL designs - A~350 W/m, B~10^{-10} Wm/(eV)^2 and D~0.0075 the RF duty factor. Table 2 compiles pertinent parameters for the ILC and XFEL. For the ILC design the total electrical cryo power is 40 MW, about half of which compeansates for the dynamic heating at 2 K.

Table 3 shows example parameters for a SC standing wave linac (ILC) and a normal-conducting TW linac (CLIC).

Table 2: XFEL and ILC linac parameters related to the cryo power needs.

	accelerating gradient [MeV/m]	duty factor D	static heat load [W/m]	dynamic heat load [W/m]
XFEL	23.6	0.65%	410	781
ILC	31.5	0.75%	337	728

Table 3: Example parameters for ILC (superconducting, standing wave) and CLIC (normal conducting, traveling wave) linacs [3,4].

Parameters		units	ILC(RDR)	CLIC(3 TeV)
Injection / final linac energy	E_{Linac}	GeV	**25 / 250**	**9/ 1500**
Acceleration gradient	E_a	MV/m	**31.5**	**100**
Average beam current	I_b	μA	42	9
Peak RF power	$P_{in\ peak}$	MW/m	**0.37**	**275**
Average RF power	$<P_{in}>$	kW/m	**2.9**	**3.7**
Initial / final horizontal emittance	ε_x	μm	8.4 / 9.4	0.38/0.66
Initial / final vertical emittance	ε_y	nm	24 / 34	4/20
RF pulse width	T_p	μs	**1565**	**0.24**
Repetition rate	F_{rep}	Hz	5	50
Number of particles in a bunch	N	10^9	20	3.7
Number of bunches / train	N_b		2625	312
Bunch spacing	T_b	ns	360	0.5
Bunch spacing per RF cycle	T_b/T_{RF}		468	6

The accelerating structure must be “filled” with RF energy prior to the bunch arrival. The relevant time is related to the “fill time” of the structure and to the average beam current during the passage of the bunch train. The voltage at the first bunch injection is chosen such that the “beam loading”, i.e. the extraction of energy through the acceleration process, exactly cancels the further voltage increase due to the continuing filling of the structure, with the result, and goal, of a constant accelerating voltage along the train. This is illustrated in Fig. 9, for ILC and for CLIC. Note that the scales in the upper and lower plot are quite different. For the ILC the total RF pulse length is about 1.5 ms, with a long fill time and a low average current, while for

CLIC the RF pulse is shorter than 250 ns, with much higher beam current in the pulse. For a given structure the fill time scales as the inverse of the pulse beam current. After the end of the beam pulse no new RF energy is fed into the structure and the stored beam energy decays. The reason for pulsing the ILC, with a duty factor $D< 1\%$, is the exorbitant cryogenic power in the case of continuous-wave (cw) operation (D=100%), highlighted by the above formula.

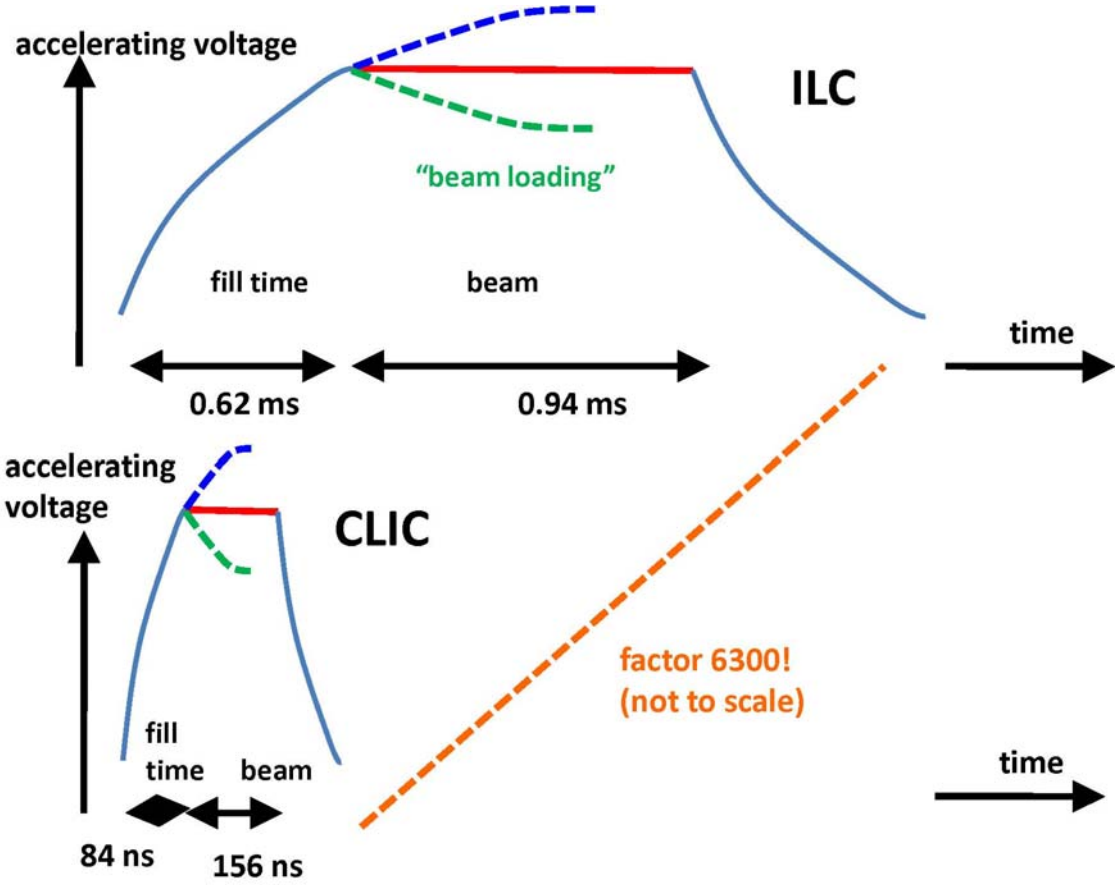

Figure 9: Time evolution of the accelerating voltage in ILC (top) and CLIC (bottom) linac structures before, during and after the passage of a bunch train.

2.5 Luminosity Challenges: Gradient and Efficiency

The electrons and positrons meeting each other at the interaction point of a linear collider pass through the linac accelerating cavities only once. The length of the linac is determined by the targeted centre-of-mass energy E_{CM} of the electron-positron collision, the RF accelerating gradient (in units of V/m) and the filling factor F, i.e. by the fraction of the linac length occupied by accelerating RF structures, or the ratio of "active" length divided by the total length. The primary challenge for future linacs is to maximize the acceleration gradient g in order to keep the collider short and the construction cost acceptable. Interestingly exactly the same challenge is encountered for medical accelerators [7]. The maximum gradient is normally

limited by field break down or other similar processes. The second challenge for the linac designer is the rf-to-beam-power conversion efficiency.

Concerning the first challenge, the acceleration gradient, we observe that the filling factor is F ~0.70 (ILC) [8], and ~0.80 (CLIC) [9]. The two-linac length is given by $2L \sim E_{CM}/(F\ g)$. For example with F~0.8, g equal to 100 MeV/m and E_{CM}=1 TeV, we obtain $2L \sim 10^{12}/(0.8\ 10^{8})$ m ~ 12.5 km.

Concerning the second challenge, the power conversion efficiency, we first take a step back. The linear collider luminosity can be written as

$$L = \frac{f_{rep} n_b N_b^2}{4\pi \sigma_x^* \sigma_y^*} H_D$$

where f_{rep} designates the linac repetition rate, n_b the number of bunches per pulse, N_b the number of particles per bunch, $\sigma^*_{x(y)}$ the horizontal (vertical) rms beam size at the collision point, and H_D a correction factor representing the combined effect of "hourglass" (change of beta function in longitudinal direction over the collision region) and disruption enhancement (due the attractive force the two colliding bunches exert on each other). The above formula can be transformed to

$$L \approx \left(\frac{5}{r_e}\right) \frac{P_{wall}}{E_b} N_\gamma \frac{\eta}{\sigma_y^*}$$

where $P_{\rm wall}$ denotes the electrical "wall-plug" power, N_γ the number of "beamstrahlung" photons emitted per electron (or positron) during the collision in the field of the opposing beam [The value of N_γ should not be much larger than 1, since it determines the quality of the differential luminosity spectrum, i.e. the fraction of the luminosity at nominal energy], E_b the beam energy, η the wall-plug-power to beam-power conversion efficiency and σ_y^* the rms vertical beam size at the collision point. The latter can be expressed as

$$\sigma_y^* = \sqrt{\frac{\varepsilon_y^N \beta_y^*}{\gamma}}$$

with ε_y^N the normalized vertical emittance, β_y^* the vertical beta function at the collision point, and γ the relativistic Lorentz factor for the electron or positron beam. In addition we can write the beam power in two different ways, namely

$$P_{beam} = f_{rep} E_b n_b N_b \text{ , or}$$

$$P_{beam} = \eta P_{wall}$$

The above relations demonstrate that the recipe for high luminosity is a small vertical normalized emittance ε_y^N, a small β_y^*, and a large efficiency η. For a given fixed wall-plug power, the luminosity is directly proportional to the conversion efficiency. Another quantity that enters in the luminosity expression is the vertical beam size σ_y^*, which should be made as small as possible by decreasing the vertical normalized emittance ε_y^N and the vertical IP beta function β_y^*. The latter should remain larger than the bunch length (because of the "hourglass effect") and the aperture of the large focusing quadrupoles must also be respected. Other limits on β_y^* are imposed by the beam-beam interaction (primary and parasitic) and by the effect of

synchrotron radiation in the final quadrupoles on the IP spot size ("Oide effect" [10]). Limits on the collider spot size are illustrated in Fig. 10.

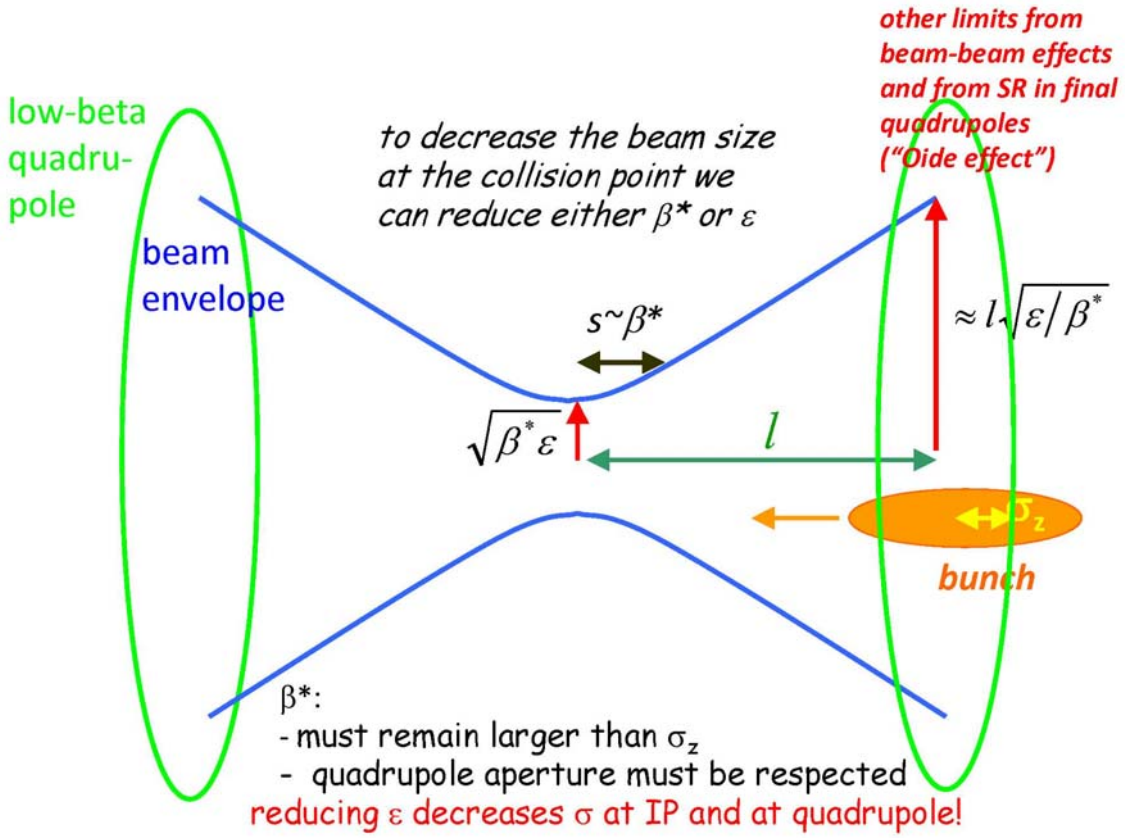

Figure 10: Limits on the linear-collider spot size.

The ILC uses SC cavities with very low losses to increase η. The ILC power conversion efficiency, including both RF and cryopower amounts to η~9.4% [8]. In the case of CLIC the efficiency is maximized by accelerating the drive beam with full beam loading and using the latter for loss-free transport of "RF" energy over long distances, yielding a total efficiency of η~7.1-7.3% [9].

2.6 SC Cavities: Preparation, RF Superconductivity and Performance

The preparation of the SC cavities is a long and complex procedure, starting with high purity niobium sheets of an Residual Resistivity Ratio (RRR) equal to 300, scanned by eddy-currents to exclude foreign material inclusions like tantalum and iron, and continuing with deep-drawing of subunits (half-cells, etc.) from niobium sheets, chemical preparation for welding, clean-room preparation, electron-beam welding according to detailed specification, a 800 °C stress annealing of the full cavity to remove hydrogen, an optional 1400°C high-temperature heat treatment with titanium getter layer, further clean-room handling like chemical etching or electro-polishing (EP) to remove the damage layer and the titanium getter layer, plus high pressure water rinsing and possibly bake out as final treatment [1].

Different from DC superconductivity, at RF frequencies the resistance is not exactly zero, but just very small. It consists of two components as

$$R_{surf} = R_{BCS} + R_{res}$$

where R_{res} denotes a residual resistance e.g. from surface impurities, and R_{BCS} is the unavoidable resistance at non-zero temperature predicted by BCS theory

$$R_{BCS} \propto \omega^2 e^{-1.76 T_c/T}$$

This latter term is related to non-superconducting electrons, which oscillate in the time-varying magnetic field and dissipate power in the material. They represent a significant heat load (1 W at 2 K corresponds to about 1 kW of primary ac power). The maximum accelerating gradient is limited by the maximum possible surface magnetic field ("superheating field", which is 180 mT for *Nb*, 400 mT for Nb_3Sn). However, despite the higher theoretical value for Nb_3Sn, the maximum accelerating gradients have so far been obtained for *Nb* (in the case of the ILC peak gradients close to 40 MV/m); see Fig. 11.

An important quality characteristic of SC cavities is the variation of their *Q* value with the accelerating gradient. Figure 12 shows such a plot for a number of "American" ILC 9-cell cavities which were tested between mid-2008 and early 2009. The five 9-cell cavities had been built by ACCEL, and then processed at JLab with one bulk EP followed by one light electro-polishing and by ultrasonic pure-water cleaning with detergent [11].

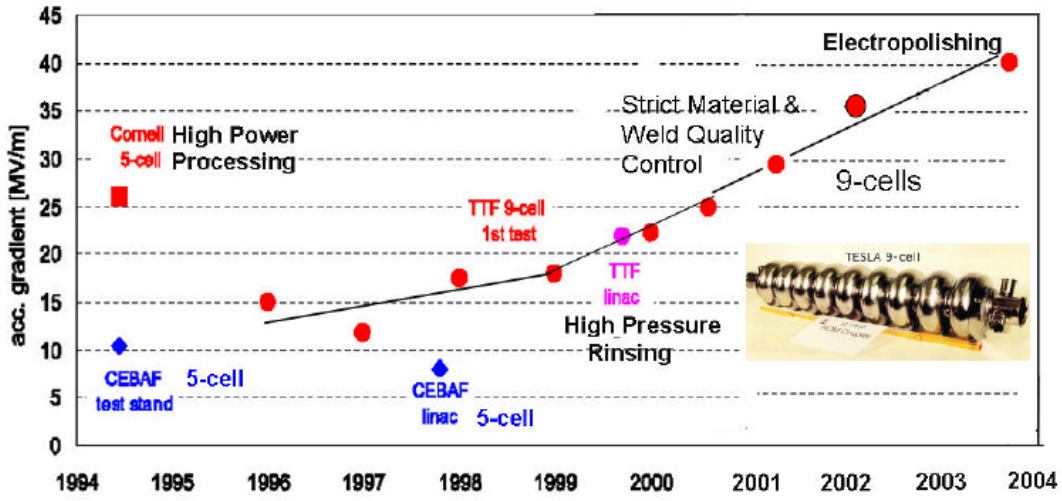

Figure 11: Progress in the SC RF accelerating field (H. Padamsee) [1].

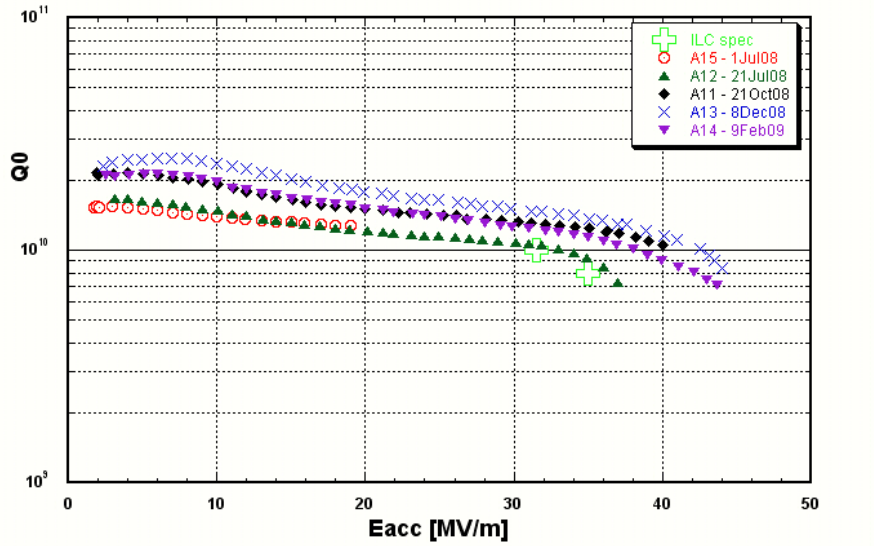

Figure 12: Quality factor versus accelerating field for 5 American 9-cell cavities in early 2009 [11].

Not all cavities achieve the same gradient. Figure 13 shows two "best gradient yield" curves for ILC cavities from November 2008 and February 2009. About 50% of the cavities reached a gradient of 35 MV/m.

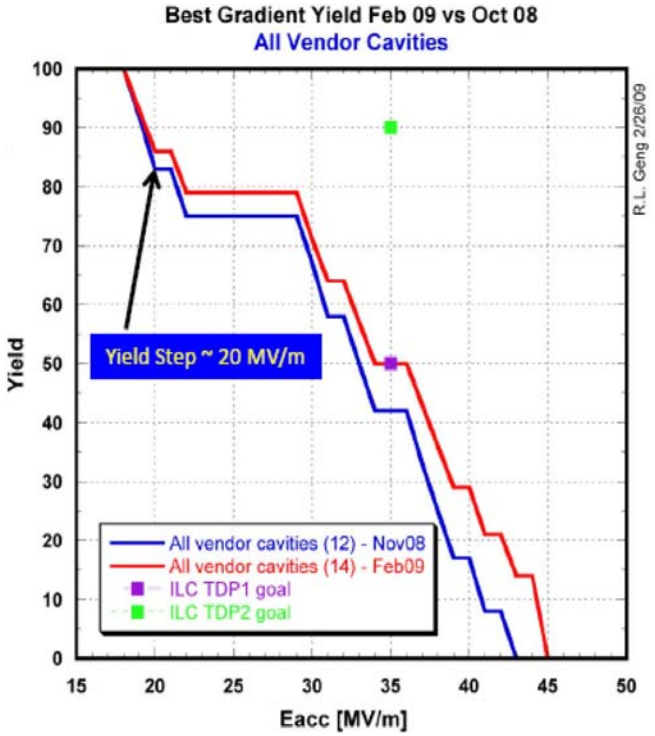

Figure 13: Yield curve for 14 9-cell SC ILC cavities processed and tested at JLab [11].

2.7 NC Cavities: Structure Optimization

The optimization of the accelerating structures of the normal conducting CLIC linac [12] takes into account beam dynamics constraints based on the simulation of the main linac, beam-delivery system, and the beam-beam collision at the IP (e.g. the bunch separation and the bunch charge depend on the linac wake fields that in turn depend on the accelerating structure), and constraints from RF breakdown and pulsed surface heating (RF), requiring a maximum temperature rise during the RF pulse below 56 K, a maximum surface electric field of less than 250 MV/m, and a limit on the RF pulse length scaling with the inverse third power of the input power (see also [13]).

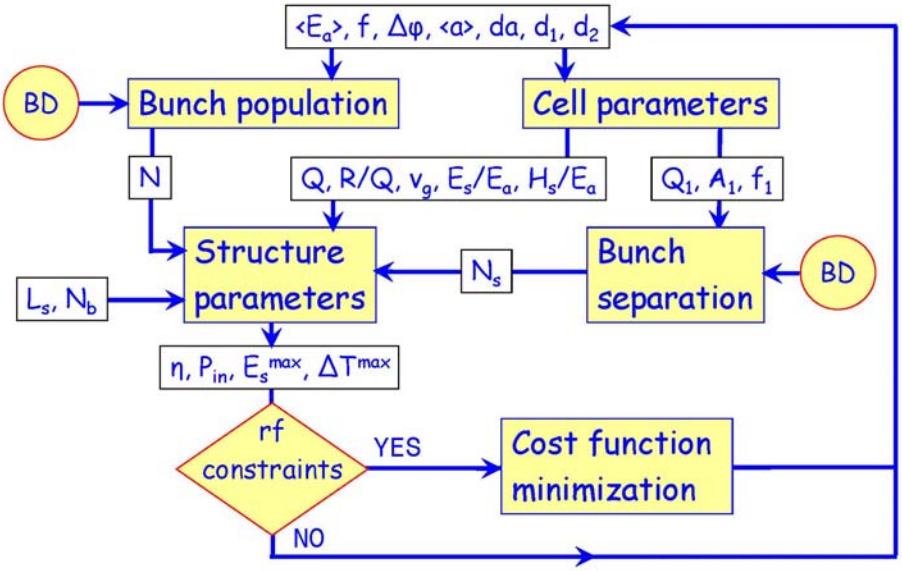

Figure 14: Flow chart of optimization procedure for the CLIC NC linac (A. Grudiev) [12].

As indicated above, combining the structure limits from RF breakdown and from RF pulse heating, and beam dynamics limits related to emittance preservation (wake fields), luminosity, bunch population, bunch spacing, and efficiency (total power), the figure of merit "luminosity per linac input power" has been optimized. The result – after analyzing 6×10^7 structures – is that the optimum CLIC parameters correspond approximately to a gradient of 100 MV at an RF frequency around 12 GHz [3]. The optimization result is illustrated in Fig. 15.

The main gradient limitation for CLIC is the RF breakdown. This term refers to a very fast dissipation of the stored RF energy, where high electric surface fields lead to an explosive electron emission and high magnetic surface fields to RF pulsed heating. Several Joules of RF energy can be absorbed in a single accelerating cell, and in the process surface melting and evaporation occur in an area of a few 100 μm^2. Strong electron emission, acoustic waves, gas desorption, X-rays and visible light are all observed during a breakdown event. The probability of breakdown during a pulse should be small. Given the length of the CLIC linac the breakdown rate should stay below 10^{-7} per meter length. Figure 16 demonstrates that this target value for the

CLIC breakdown rate has been reached by several accelerating structures designed at CERN, which were built and tested at either SLAC or KEK.

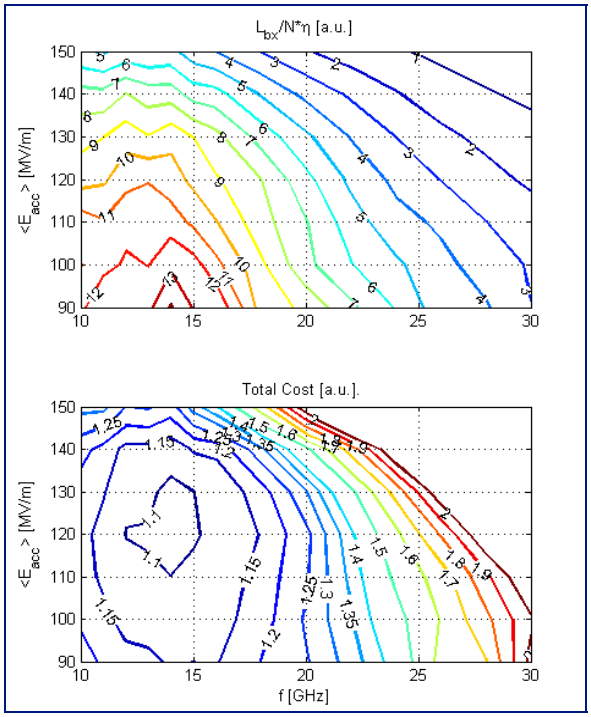

Figure 15: Contour plots for luminosity per linac input power (top) and for the total cost (bottom) in the accelerating-gradient versus RF-frequency plane [3].

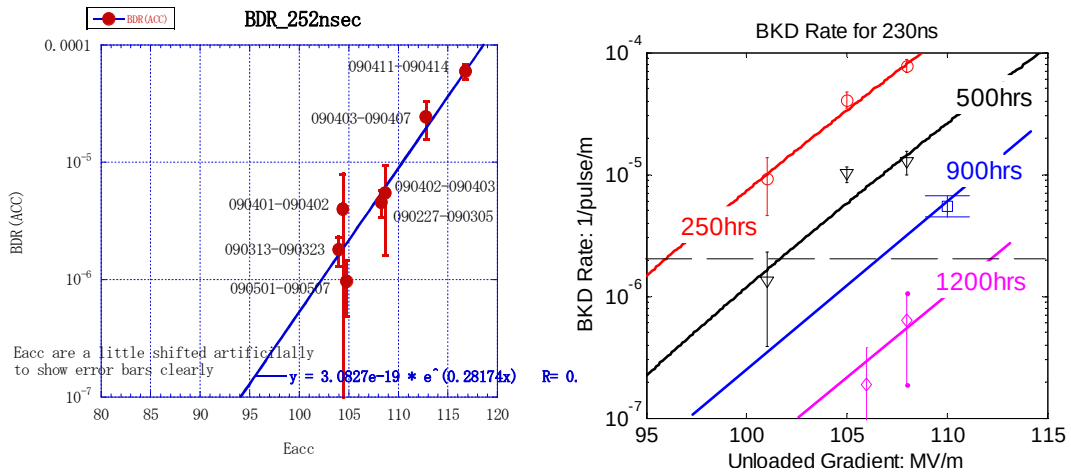

Figure 16: Nominal performance of CLIC accelerating structures (100 MV/m gradient with a breakdown rate below 10^{-7} per pulse per meter) built and tested at KEK (left) and SLAC (right) [3].

2.8 RF Power Sources

Almost since its invention in the year 1937, the primary RF power source for electron linear accelerators has been the klystron. Figure 17 demonstrates that even today there is no other device providing a comparably high average power in the 1-10 GHz frequency range. The klystron operation principle is sketched in Fig. 18, together with a photo of a 3-GHz klystron for a normal conducting linac, and a design schematic for a "multi-beam" ILC klystron. The CLIC drive beam and the ILC main beam will require 200 and about 600 klystrons, respectively.

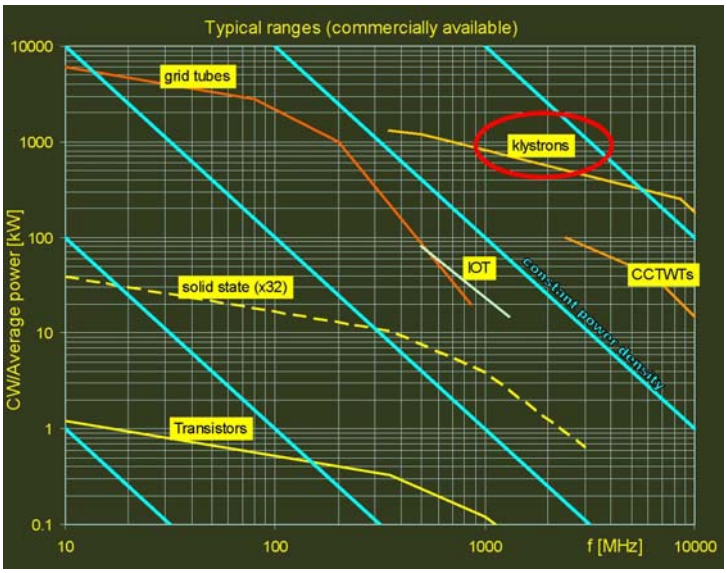

Figure 17: Average power as a function of RF frequency for different types of RF power sources [2].

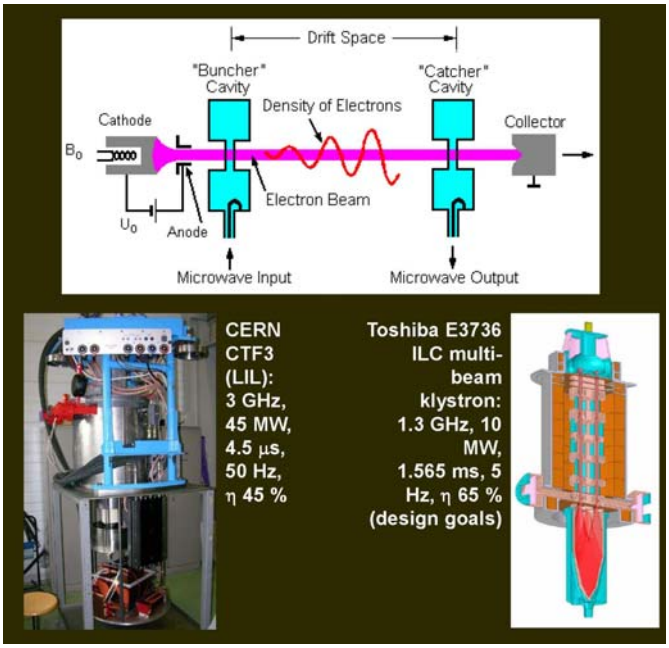

Figure 18: Klystron operating principle (top) [www.radartutorial.eu], a 3-GHz klystron for a NC 3-GHz linac at CERN (bottom left) [2], and the design of a multi-beam ILC klystron (bottom right) [8].

3. Particle Sources

A polarized electron beam can be produced with a photocathode dc gun, a (possibly polarized) positron beam with an undulator source (ILC), with a "hybrid crystal target source" (CLIC baseline, unpolarized), or with a Compton source (CLIC advanced scheme).

3.1 Electron Source

To produce an electron beam, one extracts the electrons from a metal or a semiconductor either by heating (thermionic electron gun) or by a laser. For the right choice of semiconductor and laser light one can even get polarized electrons. As soon as electrons leave the metal or seminconductor surface they are accelerated. The laser and the subsequent acceleration define the quality of the electron beam [14]. Fast acceleration by an RF or DC electric field is important to avoid dilution from "space charge" (electric repulsion between equally-charged particles which at non-ultrarelativistic energies is not balanced by the magnetic attraction). Figure 19 illustrates the working principle of a photo-cathode gun. The GaAS-GaASP superlattice developed by Nagoya University achieves the best performance in terms of quantum efficiency (electrons per photon, ~0.5%) and polarization (~90%), as is illustrated in Fig. 20.

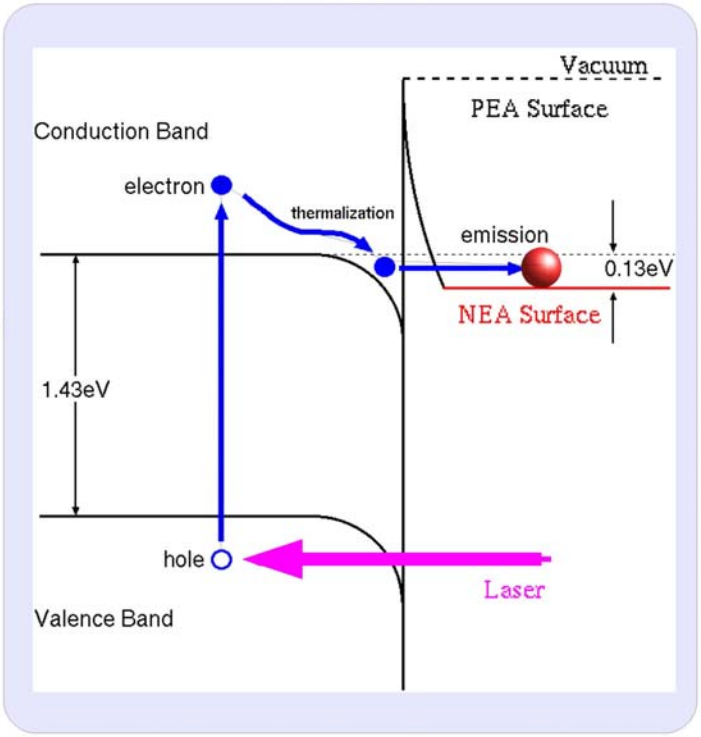

Figure 19: Energy levels and electron extraction process in a photo-cathode gun [14].

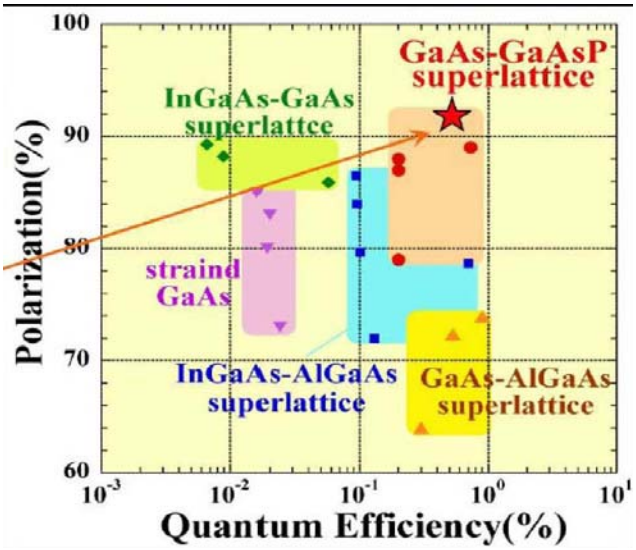

Figure 20: Operating points of various photo-cathode semiconductor superlattices in the polarization versus quantum-efficiency plane [14]. The GaAs-GaAsP superlattice with best performance was developed at Nagoya University.

The laser is one of the most important elements of the photo-cathode electron gun. The beam quality is mostly determined by the laser, for example the temporal structure (1 ns bunch length, 3 MHz repetition rate, and 0.9 ms long macropulse in the case of ILC), the normalized beam emittance (10 μm), and the polarization (with a wavelength around 800 nm). A laser system which meets the linear-collider requirements is not commercially available in the required combination of wavelength (700 nm) and average power (3 W in a macro-pulse) [15]. Figure 21 illustrates the beam temporal structure for CLIC and ILC. The design electron-source beam parameters for CLIC and ILC are compiled – and compared – in Table 4.

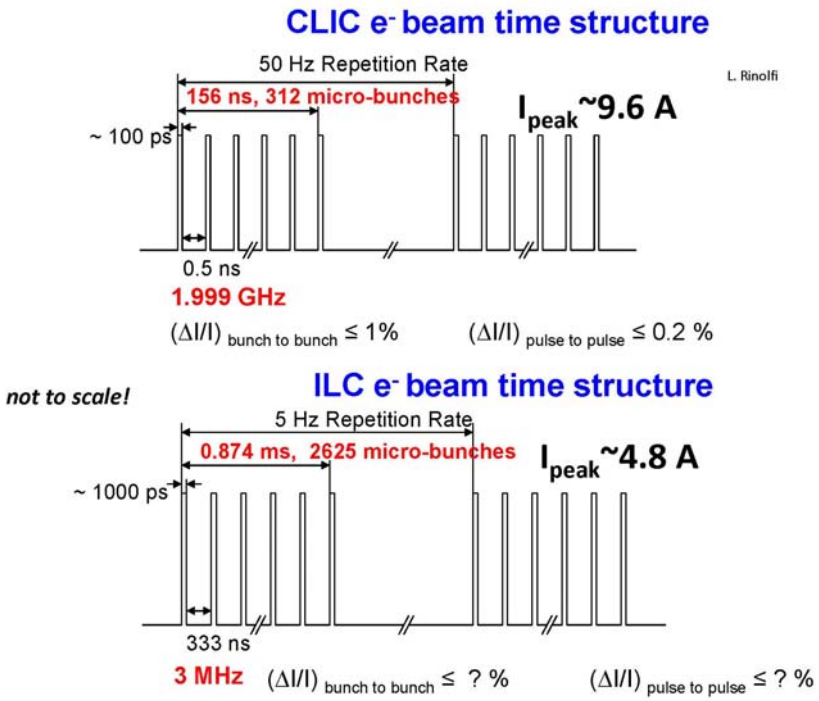

Figure 21: Beam temporal structure for CLIC [16] and ILC.

Table 4: Electron source beam parameters for CLIC [16] and ILC.

Parameters	ILC	CLIC 0.5 TeV	CLIC 3 TeV
Electrons/microbunch	~3E10	10E9	6E9
Number of microbunches	2625	354	312
Width of Microbunch	1 ns	~100 ps	~100 ps
Time between microbunches	~360 ns	500.2 ps	500.2 ps
Width of Macropulse	1 ms	177 ns	156 ns
Macropulse repetition rate	5 Hz	50 Hz	50 Hz
Charge per macropulse	~12600 nC	566 nC	300 nC
Average current from gun	63 μA	28 μA	15 μA
Peak current of microbunch	4.8 A	16 A	9.6 A
Current density (1 cm radius)	1.5 A/cm^2	5 A/cm^2	3 A/cm^2
Polarization	>80%	>80%	>80%

JLAB 100 kV electron gun
(courtesy M. Poelker)

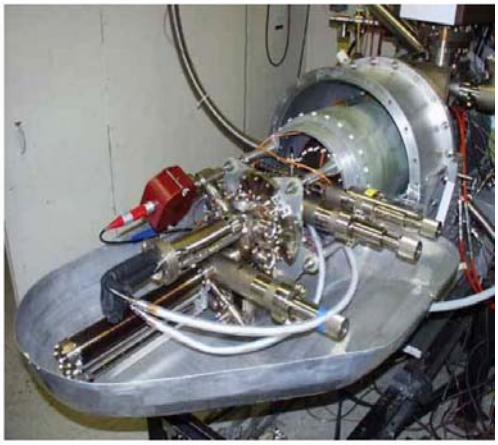

SLAC 120 kV electron gun
(courtesy J. Sheppard)

Figure 22: Example polarized electron guns at JLab (left) and SLAC (right) [16].

3.2 Positron Sources

Positrons are generated via the pair production process, $\gamma \rightarrow e+e-$, by photons (or electrons) hitting a target. In case the photons are polarized it is possible to obtain polarized positrons [17]. Among the most popular schemes or proposals for a positron source are the following four:

- bremsstrahlung from a polarized electron beam hitting an amorphous target (JLAB, SuperB)
- channeling radiation in crystals (KEK, LAL, CLIC) – not polarized
- laser Compton-backscattering source (KEK, LAL, CLIC) – polarized
- high-energy electron beam passing through a helical or planar undulator (UK, ILC) – polarized or unpolarized (Balakin & Mikhailichenko 1979 [18])

Figure 23 shows a schematic of the CLIC unpolarized hybrid-target e+ source [19,20]. In the optimized configuration, a 5-GeV e- beam is sent onto a thin crystal, with a beam spot size of about 2.5 mm. The first target crystal is 1.4 mm thick, made of tungsten, and oriented along the <111> axis where a channeling process occurs. The second target is amorpohous tungsten, 10 mm thick. The charged particles, e+ and e-, are swept off after the crystal using a magnetic field. Only γ's (with energy above 2 MeV) impinge on the amorphous target. The distance between the two targets is 2 meters. The simulated peak energy density of 0.66 GeV/mm^3 is much reduced compared to the case without the first crystal. According to a SLAC beam experiment, the target will be destroyed for peak energy densities of order ~4 GeV/mm^3.

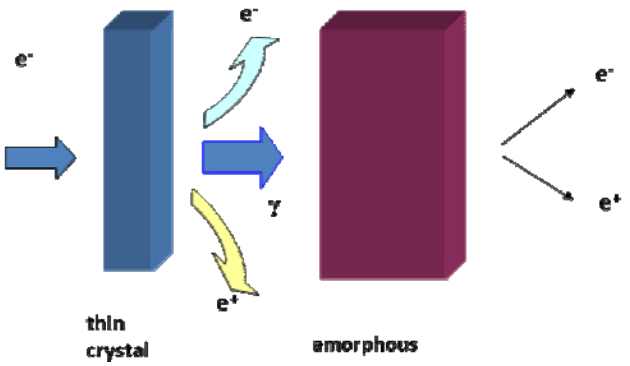

Figure 23: Schematic of CLIC unpolarized hybrid-target e+ source [16,19,20].

CLIC also pursues design studies for a polarized e+ source [16,19,20,21]. A promising concept based on Compton scattering an electron beam from an energy recovery linac off a high-energy laser pulse to generate polarized photons is illustrated in Fig. 24. Many Compton collisions are needed before obtaining the total number of e+ needed for a linear-collider bunch. To accumulate e+ coming from successive collisions, two stacking rings are used, which operate alternatingly in the stacking and damping mode [19,20,22]. A timing chart for the stacking ring operation is illustrated in the right picture of Fig. 24. From the stacking rings, the produced positron bunches are transferred to the CLIC pre-damping ring.

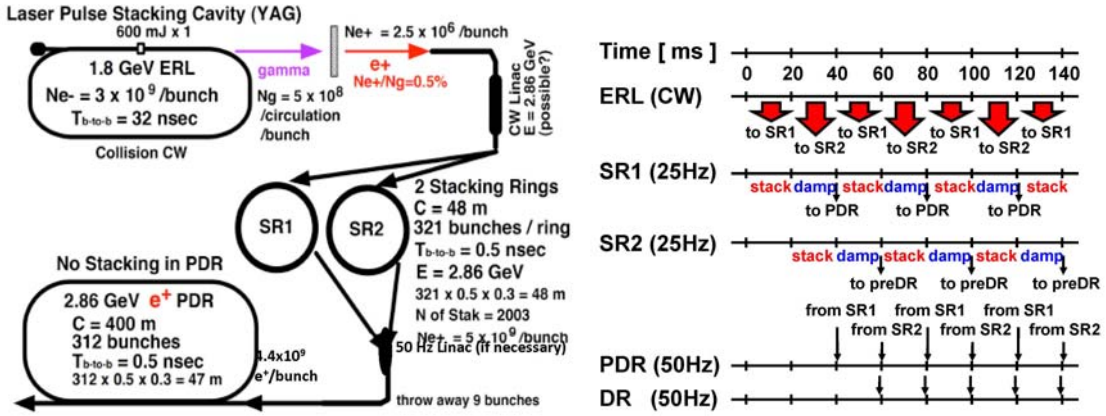

Figure 24: Scheme of CLIC polarized e+ source based on Compton scattering a laser pulse off the 1.8-GeV electron beam from an enery recovery linac (ERL) and on two stacking rings; layout of the e+ injector complex (left) and timing chart (right) [19,22].

Figure 25 shows a planar and a helical undulator, as needed for the undular based polarized e+ source, and Fig. 26 the ILC baseline source, in which a 150 GeV e- beam is sent through the undulator (the same e- beam will afterwards collide with a e+ beam). Table 5 illustrates that the number of e+ per second required for the ILC is about a factor 50 higher than what had been achieved at the Stanford Linear Collider (SLC) in the 1990's.

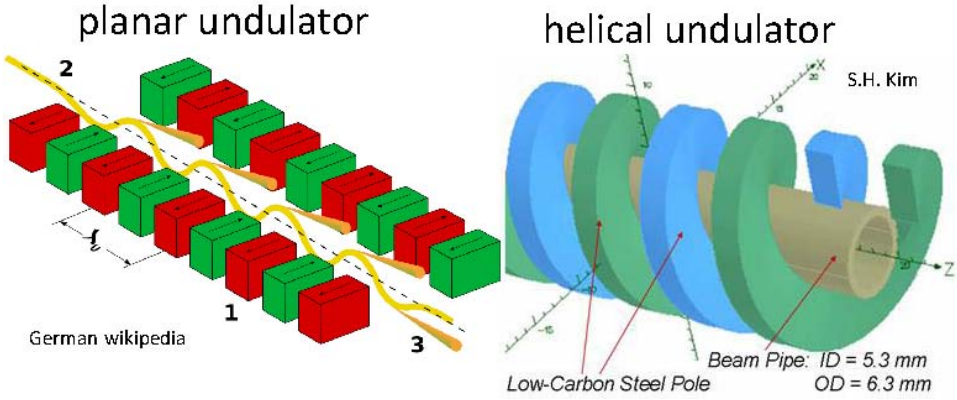

Figure: 25: Left: Periodic dipole magnet structure (1: magnets). The static magnetic field is alternating along the length of the undulator with a wavelength λ_u. Electron beam (2) traversing the periodic magnet structure are forced to undergo oscillations and radiate (3: radiation) [courtesy wikibooks]. Right: Helical undulator magnet structure – a model of a double-helix coil for the low-carbon steel poles and beam chamber. A double-helix SC coil with equal currents in opposite directions in each helix is to be inserted between the steel coils [S.H. Kim, ANL/APS/LS-311, 2006].

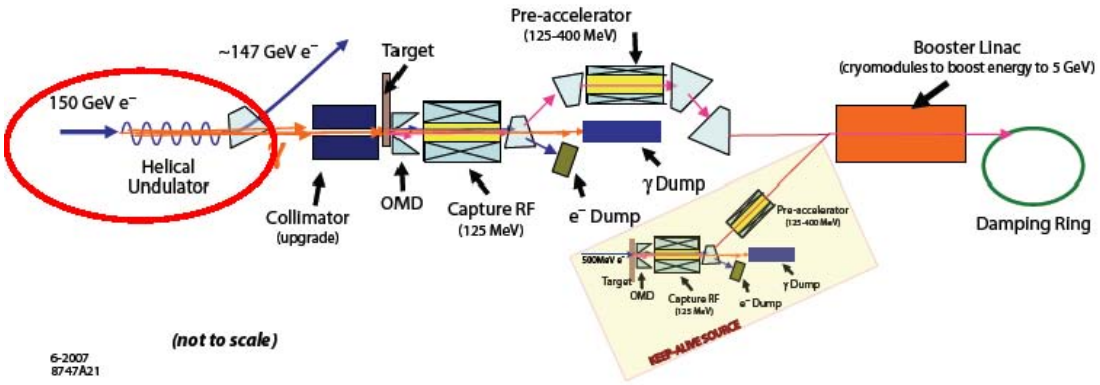

Figure 26: Schematic of the ILC baseline e+ source with SC helical undulator [23].

Table 5: Positron needs for SLC and ILC.

	SLC	ILC
positrons per bunch	$3.5\ 10^{10}$	$2\ 10^{10}$
bunches per macropulse	1	2625
macropulse rep. rate [Hz]	120	5
positrons per second	$4.2\ 10^{12}$	$2.6\ 10^{14}$

The target is one of the critical issues of the ILC baseline. Its heart piece is a rotating titanium wheel, which is exposed to eddy current heating (~ 5 kW for 1 T), to photon beam heating, and to pressure shock waves [23].

The physical processes underlying the Compton back scattering source and the helical undulator are the same, as can be seen by performing a Lorentz transformation of the undulator

field. The undulator radiation can in fact be interpreted as Compton scattering of virtual photons [24], as shown in Fig. 27.

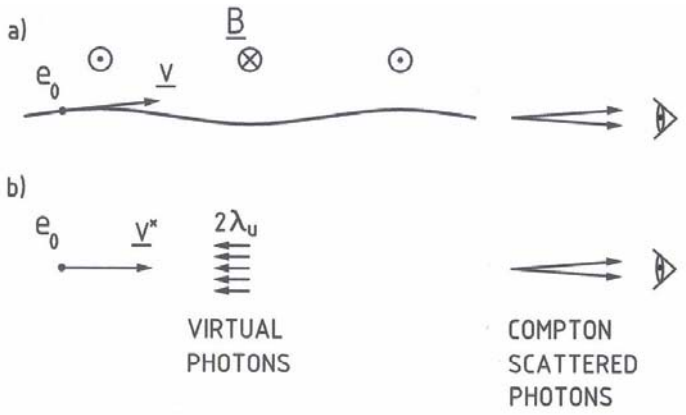

Figure 27: The radiation emitted in an undulator (a) is equivalent to the Compton scattering of virtual photons (b) [24].

The number density of the virtual photons in the equivalent picture of Fig. 27 (b) is [24]

$$n_u = \frac{B_0^2 \lambda_u}{2\mu_0 hc}$$

with B_0 the undulator magnetic field and λ_u the undulator period, and the equivalent electron velocity [24]

$$v^* = v\left(1 - \frac{K^2}{4\gamma^2}\right)$$

where

$$K = \frac{eB\lambda_u}{2\pi m_e c} = 0.934 B[\mathrm{T}]\lambda[\mathrm{cm}]$$

denotes the undulator parameter.

Despite this equivalence, in practice the two approaches have rather different implications for the accelerator design. For example, the undulator concept couples the main electron beam and the positron source, while the Compton scheme is limited in intensity, with present laser technology, and it is likely to introduce the need of "stacking".

4. Synchrotron Radiation and Damping

Accelerated charges emit electromagnetic radiation. In the case that the accelerated charge is an electron following a curved orbit in a magnetic field this radiation is called *synchrotron radiation*. One of the first comprehensive analyses of this radiation is due to Alfred Liénard in 1898. Another person who has greatly contributed to the theory of synchrotron radiation is Julian Schwinger, who had mastered the trade of classical electrodynamics in his wartime efforts on microwave propagation at the MIT Radiation Laboratory – work which had a direct impact on the highly effective new radar techniques. He later continued his pertinent studies,

and showed e.g. that synchrotron radiation contains many higher harmonics, extending into the visible range. In 1949, shortly after his papers on relativistic electrodynamics for which he went on to receive the 1965 Nobel Prize, Schwinger published another masterpiece – "On the Classical Radiation of Accelerated Electrons" [25].

4.1 Synchrotron Radiation Characteristics

Synchrotron radiation is characterized by *emission in the forward direction with a narrow angular spread*, which is due to the fast motion of the emitting electrons [26]. Synchotron radiation extends to *high frequencies*, rapidly *increasing with the energy of the emitting particles*. The peak wavelength is related to the cyclotron motion. The cyclotron frequency in the laboratory frame

$$\nu = \frac{eB}{2\pi\gamma c m_0}$$

in the electron frame becomes

$$\nu' = \frac{\gamma eB}{2\pi c m_0}$$

which, after Doppler shifting, leads to the following estimate for the emission wavelength in the laboratory frame [26]

$$\lambda \approx \frac{2\pi c^2 m_0}{2\gamma^2 eB}$$

4.2 Synchrotron Radiation Effects

The synchrotron radiation power is [27,28,29]

$$P_\gamma = \frac{cC_\gamma}{2\pi}\frac{E^4}{\rho^2}$$

With ρ the bending radius, E the beam-particle energy, and

$$C_\gamma = \frac{4\pi}{3}\frac{r_e}{\left(m_e c^2\right)^3} = 8.8460\times 10^{-5}\,\frac{\mathrm{m}}{\mathrm{GeV}^3}\,.$$

The average energy loss per turn of an indiviudal electron can be derived as

$$U_0 = \oint P_\gamma dt = \oint P_\gamma \frac{ds}{c}$$

yielding the expression

$$U_0[\mathrm{keV}] = 88.46\,\frac{E[\mathrm{GeV}]^4}{\rho[\mathrm{m}]}\,.$$

The first and second moments of the photon energy, and the average photon emission rate per unit time, are

$$\langle u \rangle = \frac{8}{15\sqrt{3}} u_c, \qquad \langle u^2 \rangle = \frac{11}{27} u_c^2$$

$$\dot{N} = \frac{15\sqrt{3}}{8} \frac{P_\gamma}{u_c}$$

where

$$u_c = \frac{3}{2} \hbar c \frac{\gamma^3}{\rho}$$

designates the "critical photon energy". The critical photon energy is defined in such a way that half the radiated power is in higher energy photons and half is in lower energy photons.

The damping due to synchrotron radiation is a classical phenomenon, which makes particles approach a fix point in the 6-D phase space, normally chosen to be the phase-space origin

$$\left(x, x', y, y', \delta = \frac{\Delta E}{E}, z \right) = (0,0,0,0,0,0)$$

The damping occurs in all 6 phase-space coordinates. The longitudinal damping in δ and z is due to the fact that the radiation power $P_\gamma(E)$ is a steep function of energy. The transverse damping has a different origin. Namely, the radiation carries transverse momentum away, while the accelerator RF-system restores only longitudinal momentum.

The transverse damping decrements $\alpha_{x,z}$ describe the exponential damping of the transverse oscillation(s) in the form

$$A_x = A_{x,0} e^{-\alpha_x t}$$

where A_x denotes the (horizontal) oscillation amplitude according to

$$x = A_x \sqrt{\beta_x} \cos\left[\omega_{\beta,x} t\right]$$

Considering a storage ring with separated function magnets (e.g. no magnets with combined dipolar and quadrupolar fields at the same location) the damping decrements are

$$\alpha_{x,y} = \frac{\langle P_\gamma \rangle}{2E}.$$

Figure 28 shows a simulation of radiation damping after injecting a beam into the CLIC Damping Ring [30].

The sum of the three damping decrements in the one longitudinal and two transverse degrees of freedom is proportional to the average synchrotron radiation power, and given by

$$\alpha_x + \alpha_y + \alpha_z = 4 \frac{\langle P_\gamma \rangle}{E}.$$

This relation is known as the Robinson's sum rule [31].

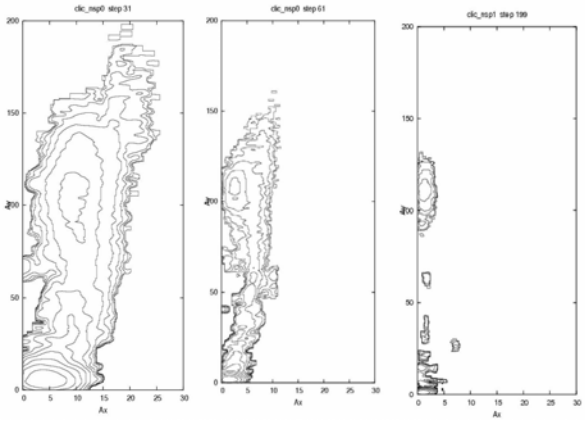

Figure 28: Simulated transverse particle distribution 3100, 6100 and 19900 turns after injection into the CLIC damping ring (transverse damping time $1/\alpha_{x,y}$ is about 2500 turns). The scale extends over 30×200 rms beam sizes at extraction. The vertical (horizontal) axis shows the vertical (horizontal) normalized amplitude A_y (A_x) [30].

In addition to the classical damping, there is also an excitation process, a quantum effect. Namely, the quantized emission of photons leads to a growth of the energy spread as

$$\left\langle \frac{dA_s^2}{dt} \right\rangle_{s,excitation} = \int_0^\infty u^2 n(u) du = \dot{\mathcal{N}} \left\langle u^2 \right\rangle$$

Also in the transverse phase space the quantum emission of photons, at locations with nonzero dispersion function *D(s)*, leads to an emittance growth. Here the emission of a photon with energy δE causes a sudden change of the reference orbit by $-D(s)\delta E/E$, which is responsible for the growth in transverse beam emittance.

The equilibrium in phase space determines the final "equilibrium emittance". It is computed by equating damping and excitation terms:

$$\left\langle \frac{dA^2}{dt} \right\rangle_{s,excitation} + \left\langle \frac{dA^2}{dt} \right\rangle_{s,damping} = 0$$

with

$$C_q = \frac{55}{32\sqrt{3}} \frac{\hbar c}{mc^2} = 3.831 \times 10^{-13} \text{ m} .$$

In the longitudinal plane this yields the equilibrium energy spread

$$\left(\frac{\sigma_E^2}{E^2} \right) = \frac{C_q \gamma^2}{2\rho}$$

which also determines the equilibrium bunch length

$$\sigma_s = \frac{\sqrt{2\pi} c}{\omega_0} \sqrt{\frac{-\eta E_0}{heV_{rf} \cos\phi_s}} \frac{\sigma_E}{E_0} .$$

In the transverse plane, the sudden change of reference orbit due to the emission of a photon of energy *u* can be expressed as

$$\delta x_\beta = -D\frac{u}{E};\quad \delta x_\beta^{'} = -D'\frac{u}{E},$$

which, on average, changes the squared oscillation amplitude by

$$\delta A_x^2 = \left(\frac{u}{E}\right)^2 \frac{1}{\beta}\left\{D^2 + \left(\beta D' - \frac{1}{2}\beta' D\right)^2\right\}.$$

This then yields the transverse qunatum excitation term

$$\left\langle \frac{dA_x^2}{dt}\right\rangle_{s,excitation} = \frac{\left\langle \dot{N}\left\langle u^2\right\rangle \mathcal{H}_x\right\rangle_s}{E_0^2}$$

with

$$\mathcal{H}(s) = \frac{1}{\beta}\left\{D^2 + \left(\beta D' - \frac{1}{2}\beta' D\right)^2\right\},$$

the "curly-H" function of Sands [29]. Equating the excitation and damping terms, one obtains the transverse equilibrium emittance

$$\varepsilon_x = \frac{C_q \gamma^2 \left\langle \mathcal{H}_x / \rho^3\right\rangle_s}{\left\langle 1/\rho^2\right\rangle_s}$$

The vertical emittance is generated either through spurious vertical dispersion via the same mechanism or through linear coupling of the horizontal motion into the vertical plane. Typically, the vertical emittance is no larger than one per cent of the horizontal emittance

$$\varepsilon_y \approx 0.01\varepsilon_x$$

and numerous beam tuning strategies attempt to make it even smaller still.

4.3 Wiggler Magnets

Wiggler magnets consist of a series of short strong dipoles with alternating polarity, in which the electron beam performs a "wiggling" motion. The wiggler magnets can generate a lot of synchrotron radiation, with little intrinsically generated dispersion, which means that they enhance the radiation damping without adding much to the excitation. This has the effect of reducing the transverse and longitudinal damping times ("damping wigglers"), and also reducing the transverse beam emittance if the wigglers are installed in a dispersion-free (straight) section of the storage ring. Wiggler magnets can consist of conventional electromagnets, permanent magnets or SC magnets. Figure 29 shows two modern examples.

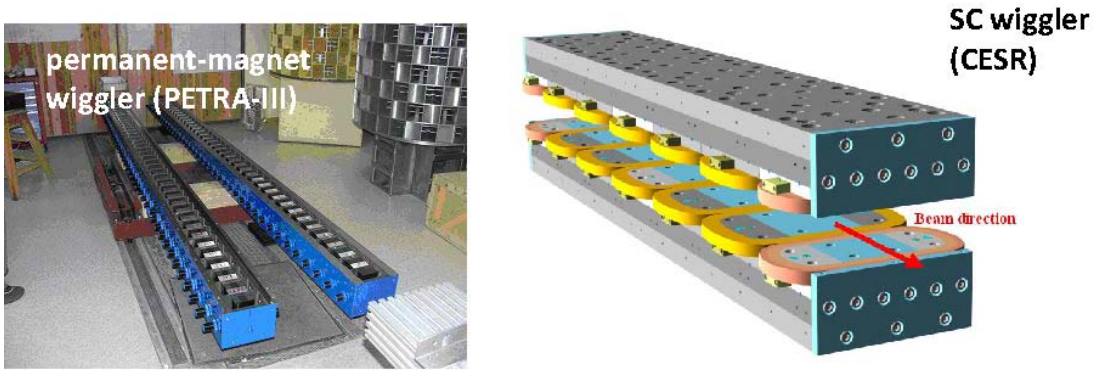

Figure 29: Two halves of a permanent wiggler magnet for the PETRA-III light source at DESY (left) [courtesy DESY, WP leader M. Tischer], and a SC wiggler of CESR (right) [courtesy Cornell].

Table 6: Parameters of SC wigglers for the CLIC damping rings proposed by BINP Novosibirsk and by Karlsruhe together with CERN.

parameters of SC CLIC wigglers	BINP	Karlsruhe / CERN
B_{peak} [T]	2.3	2.8
λ_w [mm]	50	21 or 40
beam aperture full gap [mm]	20	24
conductor type	*Nb-Ti*	Nb_3Sn
operating temperature	4.2	4.2

Adding a horizontally deflecting wiggler with N_{period} periods and a sinusoidal field pattern of period λ_w and minimum bending radius ρ_w changes the horizontal emittance compared with the case of no wigglers by the factor

$$\frac{\varepsilon_{x,w}}{\varepsilon_{x,0}} = \frac{1+\frac{4C_q}{15\pi} N_{period} \frac{\beta_{x,w}}{\varepsilon_{x,0}\rho_w} \gamma^2 \frac{\rho_0}{\rho_w} \vartheta_w^3}{1+\frac{1}{2} N_{period} \frac{\rho_0}{\rho_w} \vartheta_w}$$

$$\text{with} \quad \vartheta_w = \frac{\lambda_p}{2\pi\rho_w}$$

4.4 Recipe forAchieving Small Emittance in a Damping Ring

From the above equations and taking into account some additional constraints, the following mini recipe for the design of a low-emittance damping ring can be constructed:

1) Choose the beam energy: not too low (other emittance diluting effects become important at low energies, such as intrabeam scattering etc, and the damping time becomes longer), and not too high because the natural normalized emittance increases as the third power of the beam energy.
2) Design an optics with small value of H in the arc dipole magnets – e.g. “theoretical minimum emittance” (TME) lattice.

3) Add damping wigglers in the straight sections to increase the damping and further reduce the emittance.

4.5 Emittances in Light Sources and Linear Colliders

Figure 30 compares the target transverse emittances of the CLIC and ILC damping rings with those achieved or planned in various light sources around the world (as a function of beam energy). The Swiss Light Source (SLS) has reached a vertical emittance of 2.8 pm, which is the lowest geometrical vertical emittance, at 2.4 GeV, corresponding to ~10 nm of normalized emittance, but at lower bunch intensity than required for a linear collider. Reaching vertical emittances below 2 pm implies challenging alignment tolerances and advanced low emittance tuning schemes (coupling & vertical dispersion correction). The horizontal target emittances for the ILC and CLIC damping rings are comparable to the design value of NSLS-II (also considering that in a given ring the natural emittance increases at the third power of beam energy).

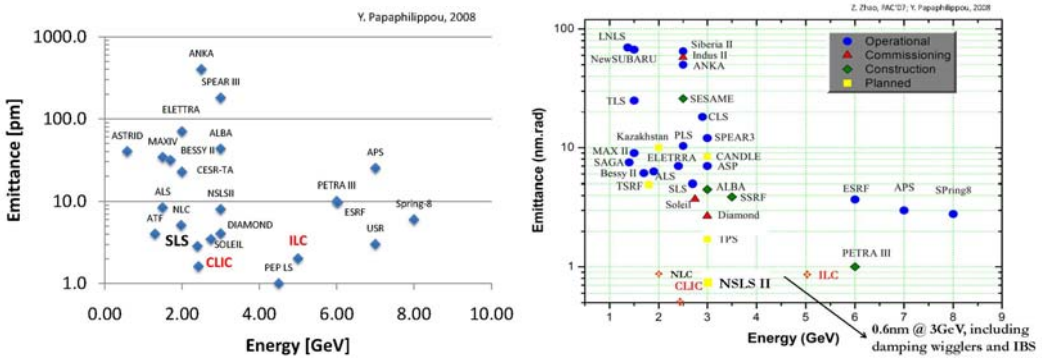

Figure 30: Vertical (left) and horizontal (right) geometric emittance as a function of beam energy for various operating and planned light sources. The parameters of the ILC and CLIC damping rings are also indicated [32,33].

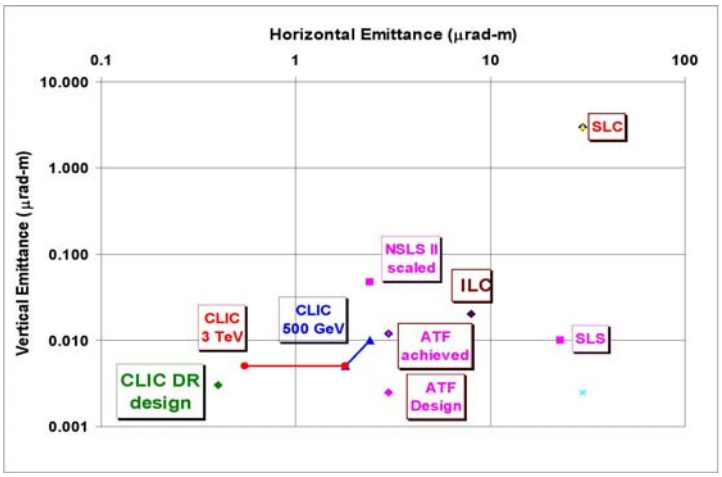

Figure 31: Normalized emittances at various damping rings and at the Swiss Light Source (SLS). The values for the SLC damping rings, ATF, and SLS have been achieved. The other points represent design values for ILC and CLIC [3].

5. Intensity Limits and Beam Stability

Accelerated particles do not move independently. Many of the limits of accelerator performance arise from interactions between beam particles. These are called "collective effects". We will describe three types of intensity limiting phenomena: (1) wake fields, which can give rise to beam break up in a linac and to single- or multi-bunch instabilities in a damping ring; (2) "electron-cloud" effects, which are most relevant for the positron beams; and (3) ion effects for electron beams.

5.1 Wake Fields

The real vacuum chamber (beam pipe) is not a perfectly conducting pipe of constant aperture. A beam passing an obstacle radiates electromagnetic fields and excites the normal modes of the object. The consequences are [34]

1) the beam loses energy;
2) energy can be transferred from head to tail of a bunch;
3) the head of the bunch can deflect the tail; and
4) energy and deflections can be transferred between bunches if there are normal mode with high Q (quality factor).

The consequences 2) - 4) can give rise to instabilities. The wake fields characterize ("are"?) the beam induced energy losses and deflections. Figure 32 contains an illustration.

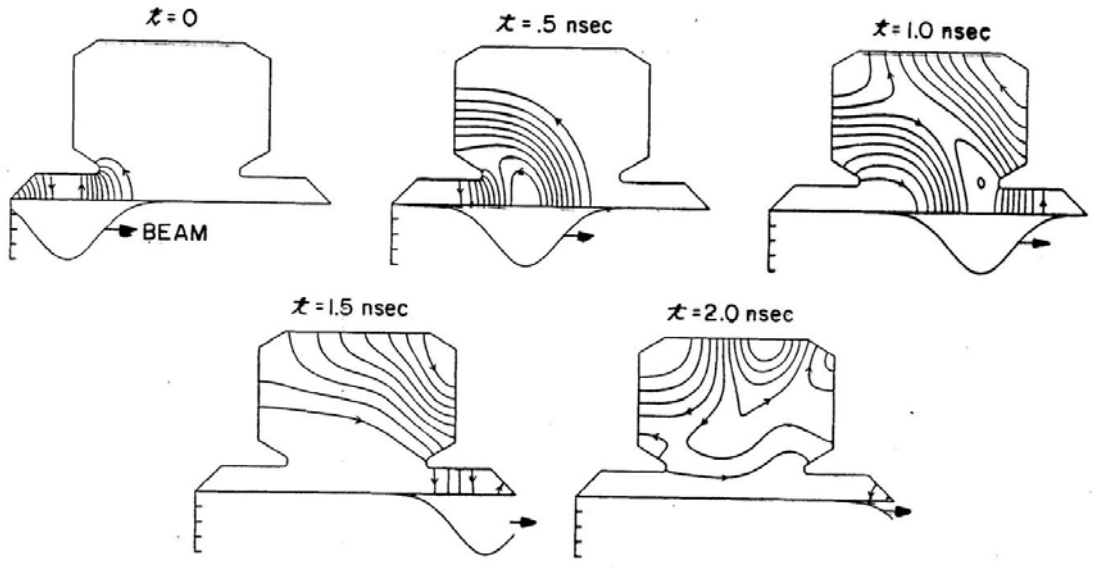

Figure 32: Simulation electrical (wake) fields induced in an RF cavity as a bunch is Gaussian passing by (simulation by T. Weiland) [34,35]. Only half of the cavity is shown. This simulation assumes azimuthal symmetry around the beam axis.

5.2 Emittance Growth in Linacs and Linear Colliders

Figure 33 presents a 1st example for the impact of wake fields, which will also illustrate the merits of a "2-particle model" for getting insight. The bottom picture shows that as two particles travel down the linac the amplitude of the second grows, since it is resonantly excited and always deflected outward through the wake fields induced by the first. As a consequence its amplitude grows. In reality, for a bunch consisting of many particles, exactly the same effect happens for the tail of the bunch, leading to emittance growth. Figure 34 (left) presents a result from a more realistic multi-particle simulation [36], revealing large growth at the bunch tail.

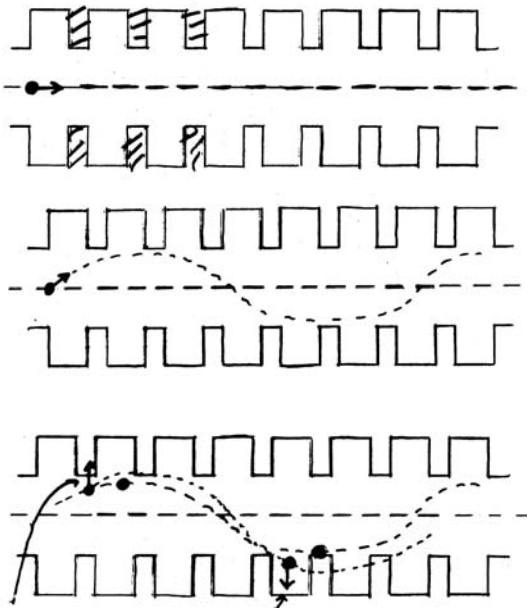

Figure 33: Single particle injected on axis traveling down the linac (top); single particle injected off-axis oscillates about the axis thanks to focusing quadrupoles surrounding the linac (centre); second particle following the first; the wake from the first deflects the second particle (bottom) [34].

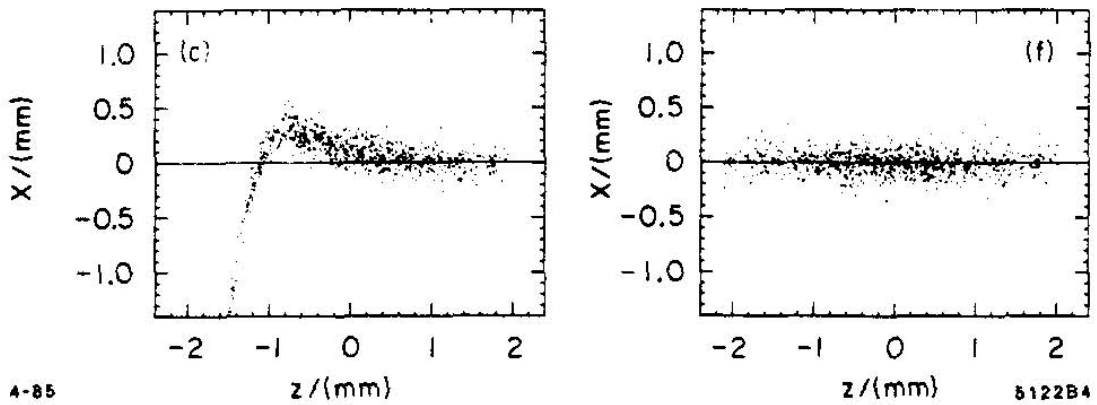

Figure 34: Multiparticle simulation of a particle bunch passing through the SLAC linac without (left) and with BNS damping (right) [36].

Possible solutions include “BNS damping” (Balakin, Novokhatsky, Smirnov [37]) and a reduction of the wake fields (by “damping” or “detuning” of the wake fields). The principle of the BNS damping can be understood from analogy with a classical driven oscillator, which has an amplitude response as a function of driving frequency as sketched in Fig. 35.

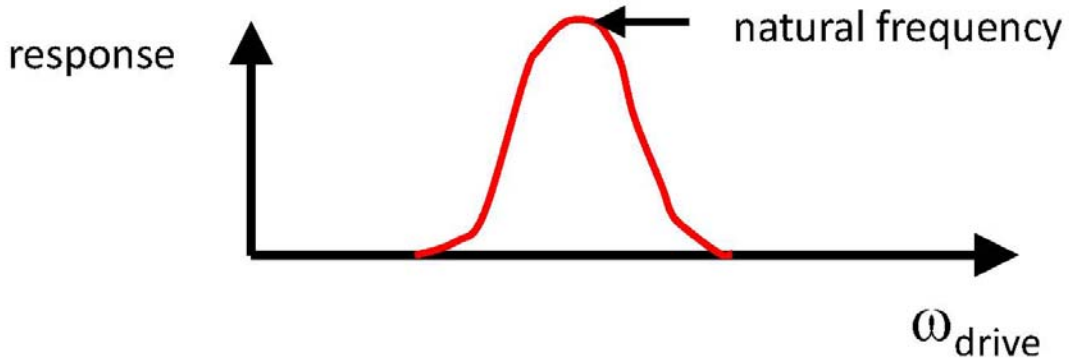

Figure 35: Sketch of amplitude response of a driven oscillator. The response is maximum if the driving frequency equals the natural frequency of the oscillator [34].

In the situation shown in Fig. 33, both head and tail particles oscillate at the same angular frequency, $\omega_{drive}=\omega_{head}$, and $\omega_{nat}=\omega_{tail}$. If $\omega_{head}\neq \omega_{tail}$ there are two effects: the response of the tail is reduced, and the initial tail oscillation beats with the driven response. Figure 34 (right) shows the stabilizing effect of a different tail frequency, for otherwise the same conditions as on the left. The frequency difference $\omega_{head}\neq \omega_{tail}$ can be achieved by RF quadrupoles (previous version of CLIC [38]) or by arranging for a different beam energy of tail and head as in the SLC (“BNS damping” [37]). The latter can be accomplished by running the bunch behind the crest of the RF wave in the early part of the linac in order to introduce a large coherent energy spread between the head and tail of the bunch.

5.3 Instabilities in Circular Accelerators

Instabilities in a circular accelerator can also be understood by using a 2-particle model. As in the linac when passing various ring elements, such as the ring RF cavities, the head produces a wake that acts on the tail particle, e.g. of charge $q/2$ each (with q the total bunch charge). However, in a ring, the head and tail interchange their position due to synchrotron oscillations, as illustrated in Fig. 36. Computing the stability of the motion over one synchrotron period, using a linear approximation to the coupled equations of motion for bunch head and tail, one finds that the synchrotron motion in a ring acts stabilizing and leads to the appearance of an instability “threshold”: up to a certain intensity the beam is stable.

.

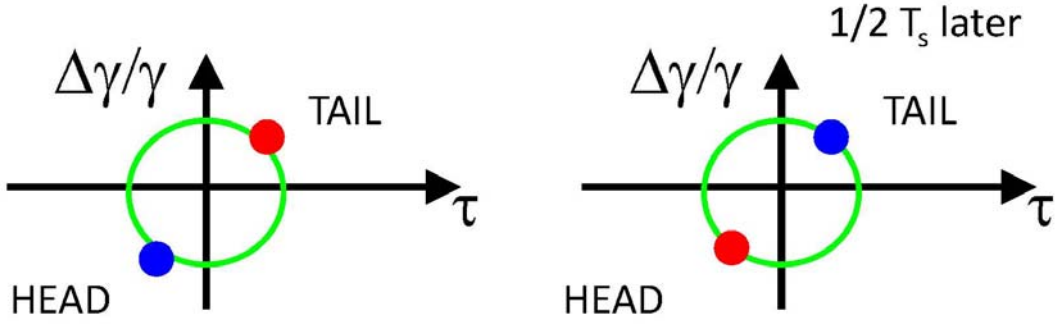

Figure 36" Longitudinal phase-space diagram showing positions of bunch head and bunch tail at a certain moment (left) and half a synchrotron period later (right) [34].

5.4 Electron-Cloud Effects

Electron-cloud effects have limited the performance of various proton and positron accelerators around the world for more than 40 years, as is illustrated in Fig. 37. An overview of electron-cloud driven instabilities and references to electron-cloud effects in the various accelerators of Fig. 37 can be found in Ref. [39].

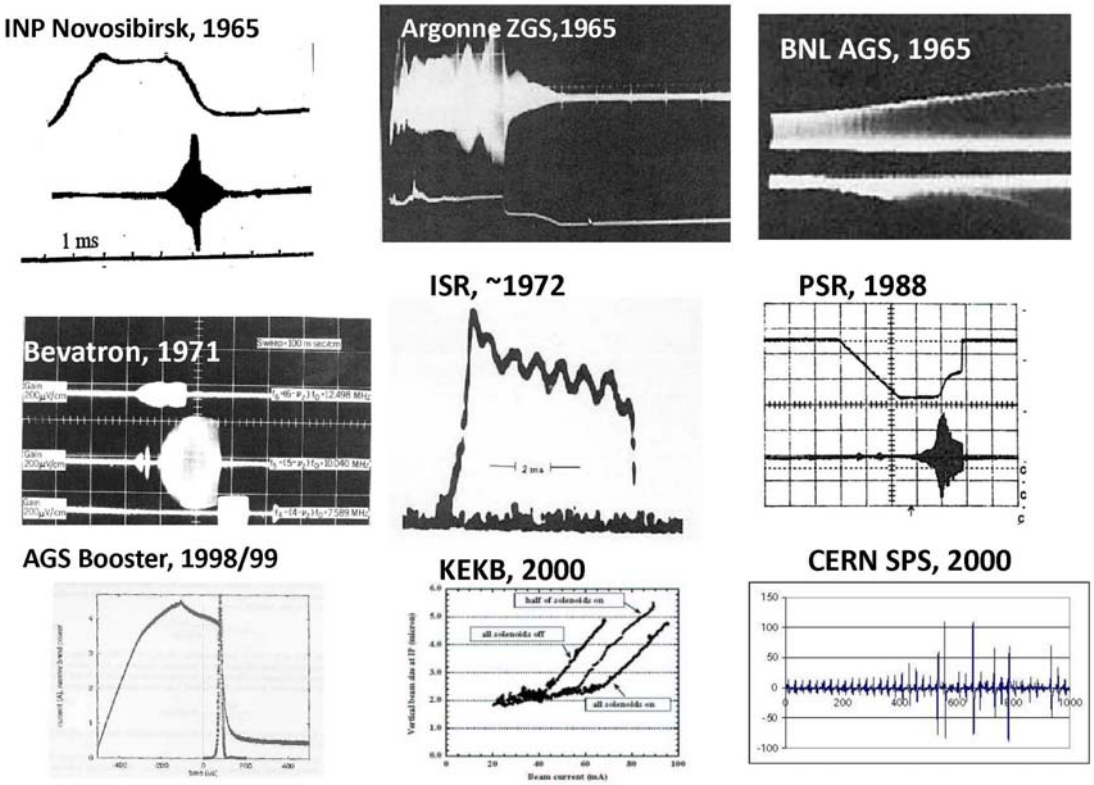

Figure 37: Electron-cloud effects observed at various accelerators around the world [39].

Where do the electrons (or ions) interacting with the beam come from? One possibility is ionization of the residual gas. The collisional ionization rate is proportional to the gas density,

and ionization cross sections are of the order 1 Mbarn, which translates to a typical number of 10^{-6} electrons or ions created per meter per beam particle. In linear colliders, due to the extremely small emittance and beam size, tunneling ionization in the collective beam field can become important at fields a few GV/m. In this case the ionization rate can be much higher as parts of the residual gas where the threshold field is exceeded are "instantly" and fully ionized during the passage of a bunch [40].

Another and larger source of electrons is photoemission when synchrotron radiation hits the chamber wall. The typical rate for this process varies from10^{-4} to 1 electron per meter per beam particle.

A third process is the avalanche build up via acceleration of electrons in the beam field followed by secondary emission at the chamber wall. If the secondary emission yield is high enough this gives rise to the build up of a true electron cloud. The equivalent process for the heavier ions leads to a "pressure bump" vacuum instability [41], in which case ion desorption by impacting ions is the amplification mechanism.

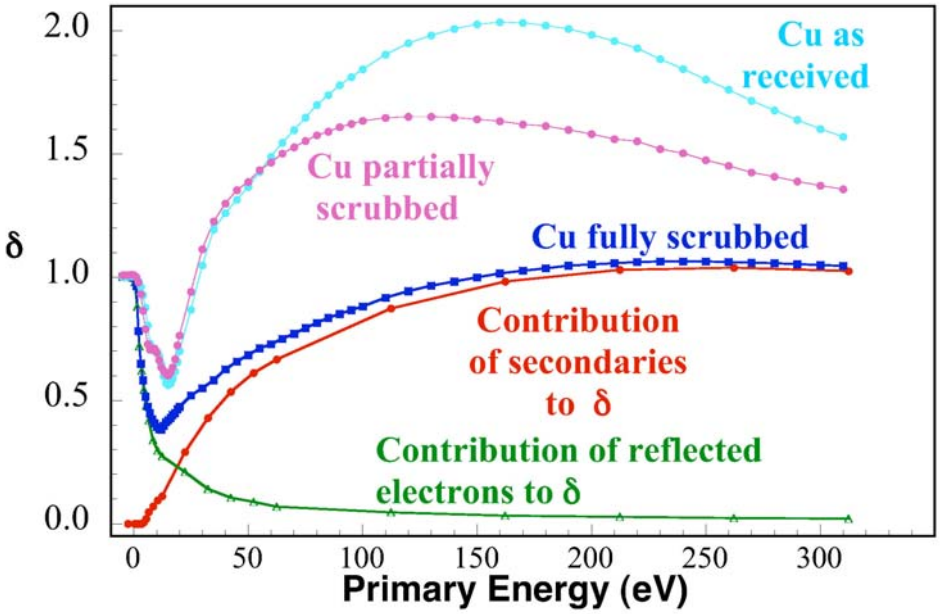

Figure 38: Measured secondary emission yield for perpendicular impact as a function of the primary electron energy for as-received, partially-scrubbed, and fully-scrubbed copper. The latter curve is decomposed into contributions from true secondaries and from elastically reflected electron, respectively, based on the measured energy spectrum [42].

The peak secondary emission yield is known as δ_{max} and the primary energy where the yield is maximum as ε_{max}. Figure 38 indicates that the probability of elastic electron reflection may approach 1 for zero incident energy, independently of δ_{max} [42].

Figure 39 shows a schematic of electron-cloud build up in the LHC. Primary photo-electrons leaving the chamber surface are accelerated in the field of the bunch that generated them through synchrotron radiation, to kinetic energies of about 200 eV. When they hit the other side of the beam pipe they then have enough energy to produce secondary electrons.

Together with additional primary photoelectrons soon an electron cloud is built up. Saturation due to the electron space charge is reached after a few tens of proton bunches.

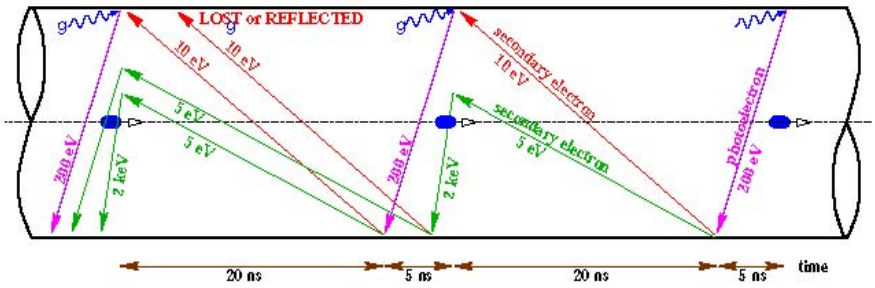

Figure 39: Schematic of electron-cloud build up in the LHC arc beam pipe due to photoemission and secondary emission (courtesy F. Ruggiero). Bunches are passing from left to right.

The electron cloud can induce a number of undesirable effects. For the LHC the electron heat load on the cold beam screen protecting the SC magnets is a main concern. In general, electron cloud build up is accompanied with a degradation of the beam vacuum and pressure rise. Electron-cloud effects more related to the beam dynamics and beam motion are coherent tune shift, single-bunch instability, multi-bunch instability, and a large incoherent tune shift. While the coherent tune shift can be used for diagnosing the electron-cloud occurrence and average electron density, the incoherent tune shift results in poor beam lifetime and emittance growth.

The threshold electron volume density for the single-bunch instability driven by an electron cloud can be estimated as [43]

$$\rho_{e,thr} \approx \frac{2\gamma Q_s}{\pi\beta_y r_0 C}$$

where on the right side we recognize the stabilizing influence of the synchrotron tune and the beam energy, and the destabilizing effect of a large circumference and a large beta function.

The bottom center picture of Fig. 37 illustrates a clear threshold of beam size blow up as a function of beam current for the KEKB LER positron ring. It also shows that installing weak solenoids around otherwise field-free regions ring increased, but did not eliminate the current threshold (the solenoid fields keeps the electrons close to the wall and prevents them from reaching the center of the beam pipe). Moreover, there is some evidence of a residual beam-size blow up below the threshold, which could be attributed to an incoherent electron-cloud effect.

In general, a multitude of countermeasures have been utilized or proposed to combat the electron-cloud build up and/or its effects, such as multi-bunch & intrabunch feedback (successful for INP PSR, Bevatron, SPS, KEKB), clearing electrodes (at ISR, BEPC, SNS), antechamber (PEP-II), TiN coating (PEP-II, PSR, SNS), high chromaticity Q' (SPS), octupoles (BEPC), solenoids (KEKB, PEP-II, SNS), and grooved surfaces (NLC, ILC).

5.5 Ion Effects

Positively charged resdiual-gas ions are attracted by and affect the electron beams. They give rise to tune shifts, incoherent tune spread, emittance growth in presence of transverse dispersion, trapped-ion multi-bunch instabilities, and fast beam-ion multi-bunch instabilities when there is a gap in the bunch train.

Heavy ions are trapped between bunches. This happens when their mass A (expressed in units of the proton mass) is large than a critical mass A_{crit}:

$$A_{crit} = \frac{N_b L_{sep} r_p}{2\sigma_y(\sigma_x + \sigma_y)}$$

The minimum gap (number of empty buckets) in the train to clear ions is of order

$$L_{g,lc} \geq 10 \times \frac{c}{\pi f_i}$$

where f_i denotes the (vertical) ion oscillation frequency in the beam potential

$$f_i = \frac{c}{2\pi}\left(\frac{2QN_b r_p}{AL_{sep}\sigma_y(\sigma_x + \sigma_y)}\right)^{1/2}$$

The incoherent tune shift due to ions in a storage of circumference C at the end of a train of n_b bunches with a bunch population of N_b each, a residual-gas temperature T and vacuum pressure p is

$$\Delta Q_{ion} \approx \frac{N_b n_b r_e C}{\pi\sqrt{(\gamma\varepsilon_x)(\gamma\varepsilon_y)}}\frac{\sigma_{ion} p}{k_B T}$$

assuming that the ions are trapped between the bunches in the train (σ_{ion} is the ionization cross section).

Simulations confirm the analytical estimates. Figure 40 shows that CO ions are cleared in a CLIC inter-train gap larger than 3 m, that hydrogen ions are overfocused even between the individual bunches of the CLIC bunch train, and that in CLIC already with a gap of 7.5 m few ions are accumulated from train to train. This required minimum gap length should be compared with the average gap between trains in the CLIC damping-ring design which is larger than 70 m.

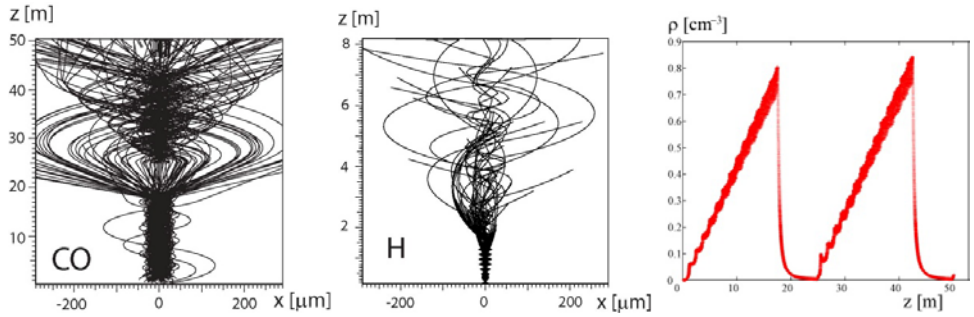

Figure 40: Simulated vertical trajectories for *CO* ions during the passage of 17.6-m long CLIC bunch trains separated by 7.5 m (left), and for *H* ions and half of the first train (centre) [44]. Simulated evolution of central ion density along a CLIC bunch train (right) [44].

Figure 41 shows an example of a trapped-ion instability that was observed at the SLC damping ring, where the injected beam was large enough that various ion species were trapped from turn to turn.

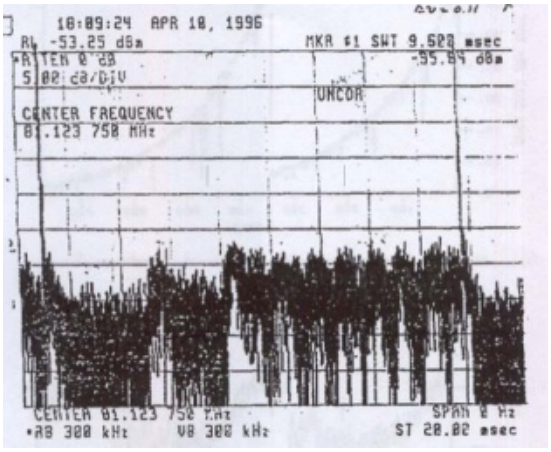

Figure 41: Trapped-ion instability observed at the SLC Damping Ring (DR) [45]. Shown is the time dependence of the amplitude of the $(13f_0\text{-}f_b)$ vertical sideband during a 16.6 ms store at the SLC DR with only two bunches under poor vacuum conditions in 1996. The two tall peaks are the injections. The irregular bursts correspond to the ion-driven instability.

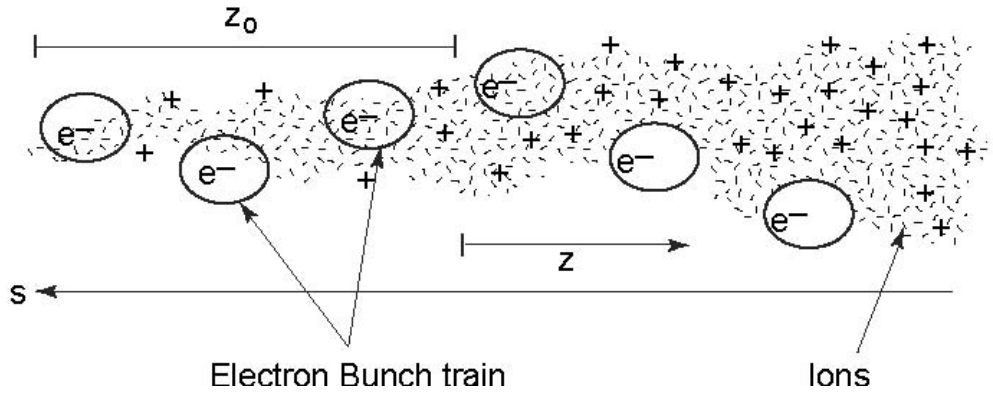

Figure 42: Schematic of the single-pass fast beam-ion instability [46].

If there is a clearing gap in the bunch train, the trapped-ion instability no longer occurs. Instead there is the possibility of a "fast beam-ion instability" [46], as illustrated in Fig. 42. Taking into account the ion oscillation decoherence (primarily due to the variation of the vertical ion oscillaiton frequency with horizontal position) and the spatial variation of the ion oscillation frequency around the ring or across the optical cell of the lattice, one finds that the instability assumes an exponential growth with rise time [47]

$$\tau_{FBII2} \approx \frac{\gamma\sigma_y\sigma_x}{N_b n_b c r_e \beta_y \sigma_{ion}} \left(\frac{k_B T}{p}\right) \sqrt{\frac{8}{\pi}} \left(\frac{\sigma_{f_i}}{f_i}\right)$$

where σ_{fi}/f_i designates the relative ion frequency spread (around the ring). For many operating (or past) storage rings like ALS, PLS, PEP-II, KEKB HER, ESRF, and Spring-8 the growth time is of order 1 ms.

Table 7: Ion effects in various damping-ring designs proposed for ILC and CLIC (2006 parameters) for an average *CO* vacuum pressure of 0.2 nTorr [44].

ring	ILC OTW			ILC OCS			ILC TESLA			CLIC	
	arc	wiggler	str.	arc	wiggler	str.	arc	wiggler	str.	arc	wiggler
critical mass	8	151	8	6	69	24	44	285	1	15	9
vert. ion freq. [MHz]	33.4	144	33.3	19.2	66.5	39.2	16.4	41.5	2.8	360	275
min. gap $L_{g,cl}$ [m]	29	7	29	50	14	24	58	23	340	2.7	3.5
ion dens. ρ_{ion} [cm^{-3}]	0.86	16.9	0.90	0.46	5.7	2.0	1.1	7.3	0.06	0.58	0.34
exponential rise time	22	6	6	32	9	6	18	5	102	189	185
at train end [μs]	[average rise time 10]			[average rise time 11]			[average rise time 47]			[av. rise t. 187]	
incoherent tune shift	0.11	0.055	0.28	0.13	0.02	0.64	0.154	0.145	0.19	0.001	0.001
at train end ΔQ_y	[total $\Delta Q = 0.44$]			[total $\Delta Q = 0.79$]			[total $\Delta Q = 0.49$]			[total 0.0026]	

Predicted ion effects for different versions of the ILC damping ring and for the CLIC damping ring are summarized in Table 7. The table demonstrates that ion effects are a potentially serious issue for the ILC damping rings. Different incarnations of the ILC damping rings feature average ion-instability rise times between 10 and 50 μs. At realistic *CO* pressure values of 0.1-0.2 nTorr, the ion-induced tune shift approaches integer values, and the fast beam-ion instability exponential rise time is about 1 turn (10-50 μs). For CLIC, ion effects appear more benign, with tune shift of a few 0.001 and a rise time of a few hundred turns. A possible solution for ILC is to split the beam into about 100 trains separated by large gaps of 20-100 m in length each. Simulations also suggest that ions which are overfocused during a bunch-train passage may not be lost, but instead form an "ion cloud" at large amplitudes around the beam.

6. Beam Delivery

The functions of the beam delivery system are:

- demagnification to small spot size ("final focus") and collision with opposing beam;
- removal of beam halo and detector background control;
- machine protection;
- emittance diagnostics, correction & IP tuning;
- preservation of beam quality; and
- beam disposal.

6.1 Final-Focus System

One of the major challenges of the final-focus design is the chromatic correction. The beam from the linac has a fairly large energy spread, typically δ_{rms}~0.1-0.3%. Without any correction the chromaticity of the final-focus system, together with the large energy spread, will increase the interaction-point vertical spot size above the spot-size obtained for an idea mono-chromatic beam, σ^*_{y0}, by a factor

$$\frac{\Delta\sigma_y^*}{\sigma_{y0}^*} = \xi\delta_{rms}$$

$$\sigma_{y0}^* \equiv \sqrt{\beta_y^*\varepsilon_y}$$

where ξ , the final-focus "chromaticity," is a large number, with a value of several thousand at least. The problem of the final-focus chromaticity is illustrated schematically in Fig. 43.

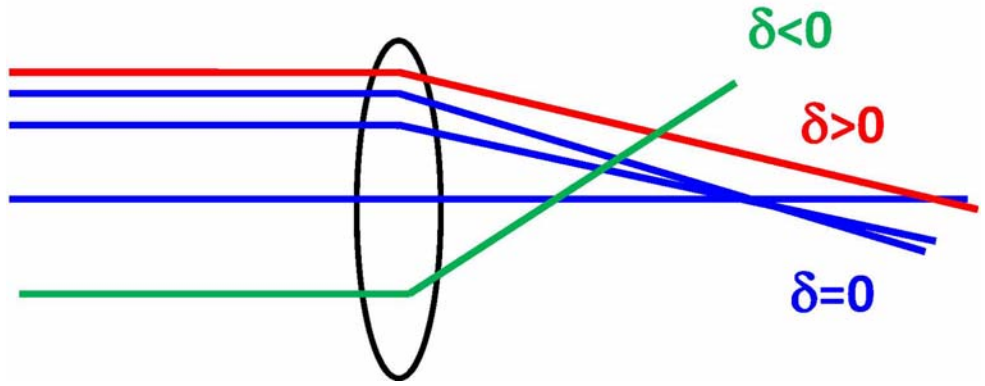

Figure 43: Schematic of final-focus chromaticity. Without correction the focal length of the final quadrupole(s) differs for particles of slightly different energy (or relative momentum offset δ=ΔE/E).

The IP chromaticity of the final focus system, including contributions from sextupoles (of strength K_s) at dispersive locations (dispersion function D) is written as [48]

$$\xi_{FF} = \int_{IP}\left[K_Q - DK_S\right]\beta\ \sin^2\left(\varphi_{y,IP\to s}\right)ds$$

We note that this differs from the storage-ring definition by a factor 2π and by the explicit dependence on the betatron phase advance to the interaction point. Table 8 shows example parameters, including β^*, chromaticity and rms beam size, for various final-focus designs.

Table 8: Chromaticity in selected final-focus systems [49].

project	status	β_y^* [mm]	L^* [m]	L^*/β_y^*	ξ_y	σ_y^* [nm]
SLC	measured	2.0	2.2	1100	**6000**	500
FFTB	design	0.1	0.4	4000	17000	60
FFTB	measured	0.167	0.4	2400	**10000**	70
ATF2	design	0.1	1.0	10000	**19000**	37
ATF2 pushed	proposed	0.05	1.0	20000	**38000**	<26
ATF2 pushed++	proposed	0.025	1.0	40000	**76000**	<20
CLIC 500 GeV	design	0.2	4.3	21500	**35000**	3
CLIC 3 TeV	design	0.09	3.5	39000	**63000**	1
ILC	design	0.4	3.5	8750	**15000**	6
ILC pushed	design	0.2	3.5	17500	**30000**	4

For a long time, final-focus systems have been designed with a non-local chromaticity compensation as for the Final Focus Test Beam (FFTB) at SLAC. In such globally corrected systems, the chromaticity is compensated by sextupoles located in dedicated "chromatic-correction" sections. Geometrical aberrations are canceled by arranging sextupoles in pairs separated by an optical negative identity transform (*-I*) [50,51]. The chromaticity arising at the final quadrupole doublet is "pre-compensated" ~1000-m upstream. Figure 44 shows an example system of this type.

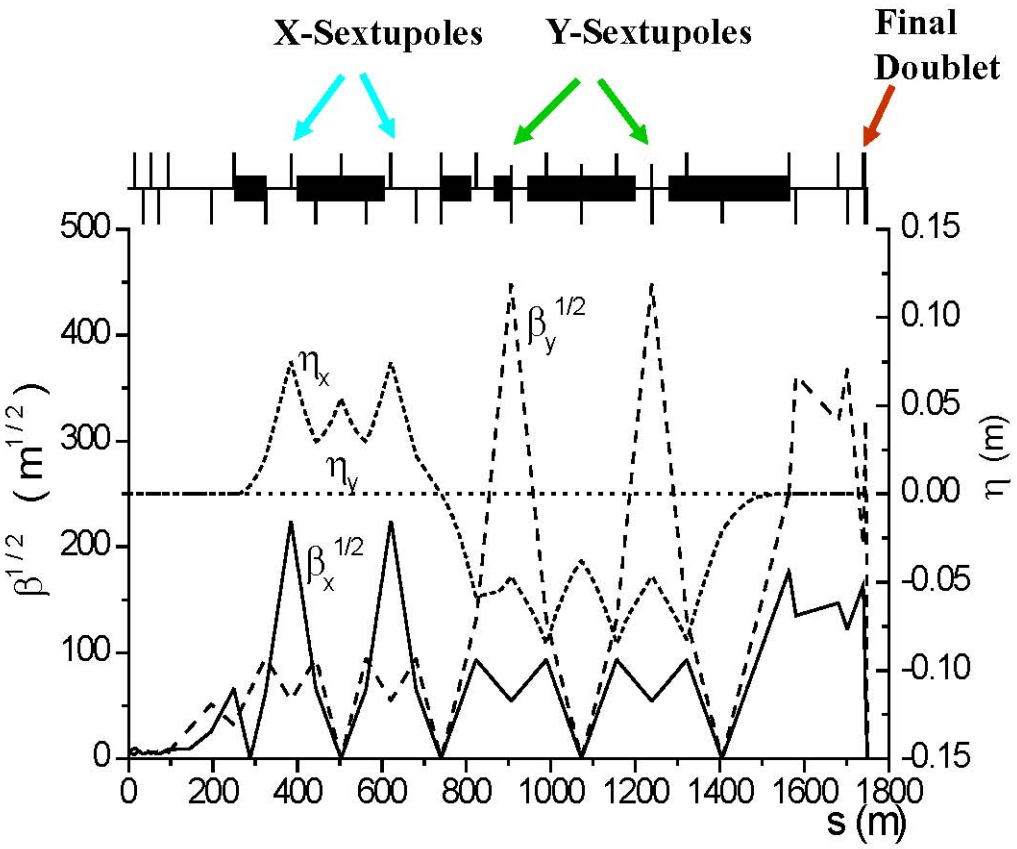

Figure 44: Conventional final focus system for a high-energy linear collider [52].

Considering two sextupoles separated by a *–I*, with equal value of the dispersion function D_i, and limiting the discussion to horizontal motion plus momentum errors only, it can be shown that the horizontal slope of a particle after the second sextupole is given in terms of the initial slope just prior to the first sextupole, x_i', its momentum error δ, and the two sextupole strengths $K_{s,1}$ and $K_{s,2}$ as [53]

$$x_2' = -x_i' - \frac{1}{2}K_{s,1}\left(x_\beta^2 + 2x_\beta D_i\delta + D_i^2\delta^2\right) + \frac{1}{2}K_{s,2}\left(x_{\beta,i}^2 - 2x_\beta D_i\delta + D_i^2\delta^2\right)$$

Choosing $K_{s,1} = K_{s,2} \equiv K_s$ this simplifies to $x_2' = -x_i' - 2K_s x_\beta D_i\delta$ which shows that the *–I* sextupole pair (aside from changing the sign of the slope) generates only linear chromaticity, but no other e.g. geometric aberrations. In reality the *–I* transform is not perfect, but changes

with δ. This gives rise to higher order chromo-geometric aberrations which ultimately limit the momentum bandwidth of the final focus.

The conventional modular final-focus system is long and shows an unfavorable scaling with the beam energy. The poor scaling is primarily caused by the stochastic component of the synchrotron radiation emitted between the sextupoles and between the sextupoles and final doublet, which leads to a random change in particle energy between the chromatic pre-compensation and the chromaticity of the final doublet, which compromises the chromatic correction and calls for weak bending magnets. The main features determining the poor energy scaling are indicated in Fig. 45.

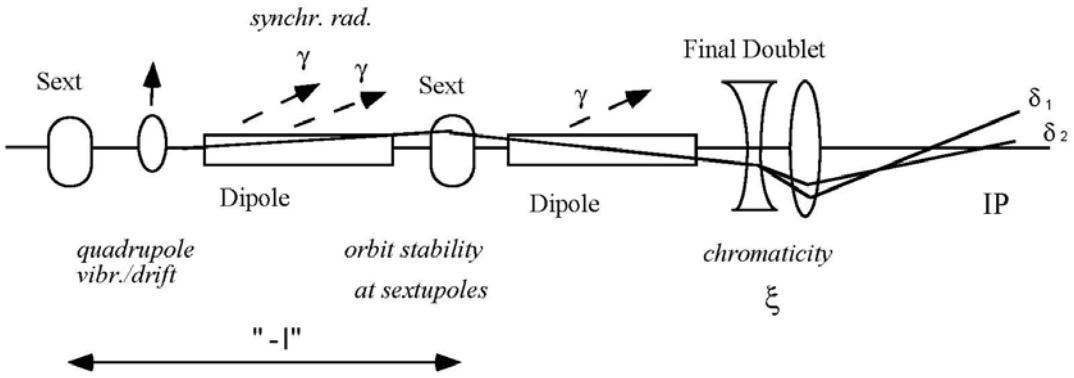

Figure 45: Schematic of a conventional final focus with stability tolerances and synchrotron radiation that determine the length scaling with energy [54].

Around the year 2000, a novel more "compact" final focus system with semi-local correction has been proposed by Raimondi and Seryi [55]. Here the chromaticity is cancelled locally by two sextupoles interleaved with the final doublet quadrupoles, and an upstream bending magnets generates dispersion across the final doublet. The geometric aberrations of the FD sextupoles are cancelled by two more sextupoles placed in phase with the former and located upstream of the bend. The layout of such a compact final focus is sketched in Fig. 46. The value of dispersion in the final doublet is usually chosen so that it does not increase the beam size by more than 10-20% for a typical beam energy spread.

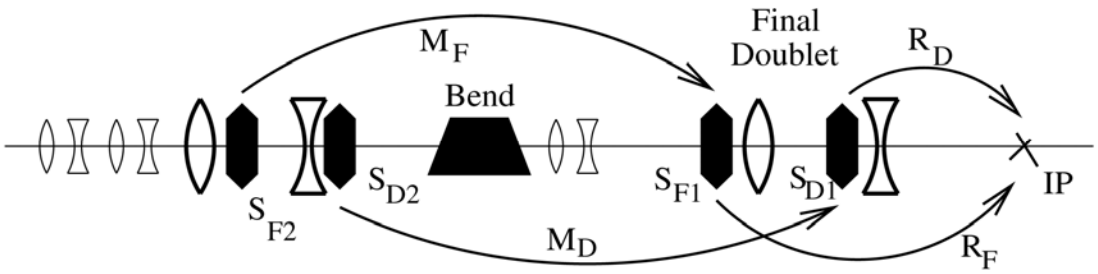

Figure 46: Schematic of a "compact" final focus with "semi-local" chromatic correction [55].

There is one subtlety in the design of the horizontal chromatic correction: If one sets the local focusing sextupole so as to cancel the chromaticity of the adjacent focusing quadrupole of

the final doublet, half of the second order dispersion remains at the interaction point. The solution adopted is to produce as much horizontal chromaticity in the upstream matching section as in the final doublet, so that the horizontal sextupole is excited twice stronger and in doing so the second order dispersion is cancelled as well [52]. This is why the chromatic correction in the less critical horizontal plane is not local, but "semi-local," even for the compact system.

A 250-GeV final focus with (semi-)local chromaticity compensation and of the same performance as a conventional modular system can be ~300 m long, or about 6 times shorter than the equivalent conventional system [52]. The momentum bandwidth is even superior to that of the conventional design, exceeding ±1%, thanks to the greater locality of the chromatic correction.

6.2 Collimation

In a linear collider, the beam normally is not of the ideal (e.g. Gaussian) shape. Beam tails can develop through a number of processes, such as

- beam-gas Coulomb scattering
- beam-gas bremsstrahlung
- Compton scattering off thermal photons
- linac wake fields
- halo from the source or from damping rings, and
- halo from ring-to-linac transport and bunch compression,…

Figure 47 shows a beam distribution measured at the end of the SLAC linac to illustrate this point.

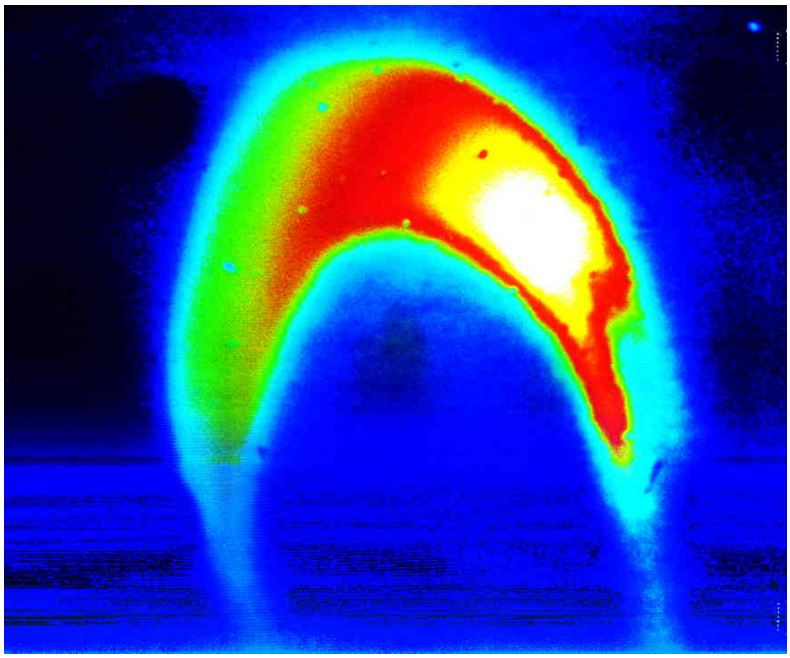

Figure 47: Beam distribution measured at the end of the SLAC linac (projection onto the x-y plane) [56].

At the SLC background had not been considered a concern in the design phase (or, at least, the background chapter in the SLC Design Handbook had been left empty). The reality proved different. Background greatly compromised the SLC performance in the first years of operation. Muons, synchrotron radiation, and electromagnetic showers were all problems and caused background in the particle physics detector(s). More and more collimators were added over the years upstream of the final focus. Magnetized toroids were placed between collimators and collision points to reduce the number of muons reaching the detector. And it proved difficult to model and to understand the halo.

Sensitized by the SLC experience, enormous efforts have been made in the TeV-scale linear collider designs to control beam tails and suppress background with the help of additional long beam-line segments, called the collimation section(s). Collimation is done using combinations of thin spoilers (for survival) and thicker absorbers, in both betatron phases and in energy. The scattering off the thin spoiler increases the size of the scattered beam at the subsequent absorbers in order to prevent damage.

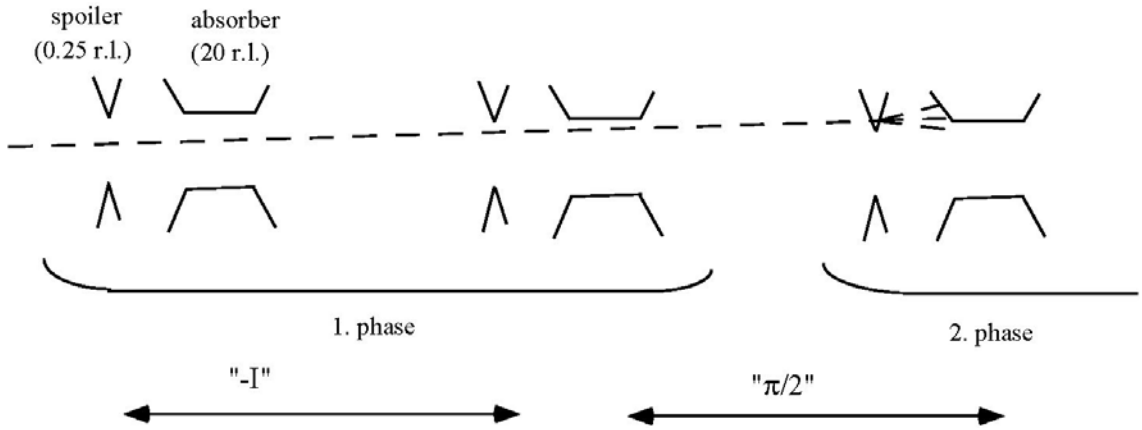

Figure 48: Schematic collimation system for future linear colliders consisting of spoiler and absorber pairs [53].

6.3 Total Beam Delivery

The total ILC 500-GeV beam delivery system has a length of about 2.4 km, including upstream emittance diagnostics and coupling correction sections [52]. Figure 49 shows the collimation and the final focus, which together amount to about 1.6 km (per beam), or 2/3 of the total. The ILC betatron spoilers survive the impact up to two bunches (after which the rest of the beam should be dumped before arriving at the collimators). The energy-spoiler survives several bunches. There is one spoiler per final-doublet or IP betatron phase.

Figure 50 presents the optics of the full 3-TeV beam delivery system for CLIC, with a length of 2.8 km per beam. In the case of CLIC, energy collimation is put first since frequent energy errors are expected both from the SLC experience and in view of the CLIC acceleration scheme. In addition, the beam size at the energy spoiler is chosen so large that the latter can survive the impact of a full CLIC beam pulse, which is required for reasons of machine protection.

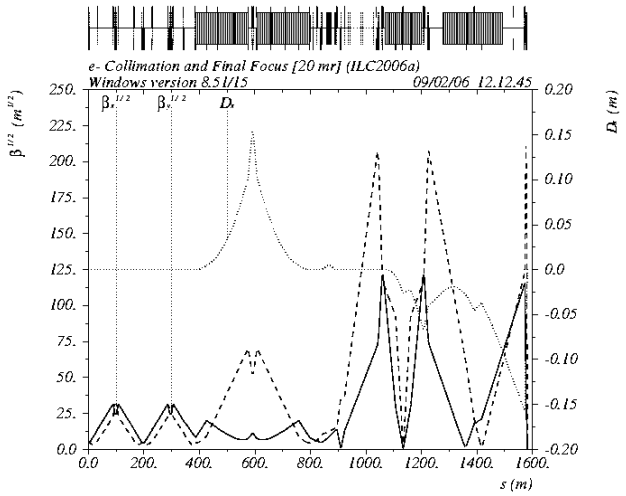

Figure 49: Optics of the ILC beam delivery system – collimation section and final focus [52].

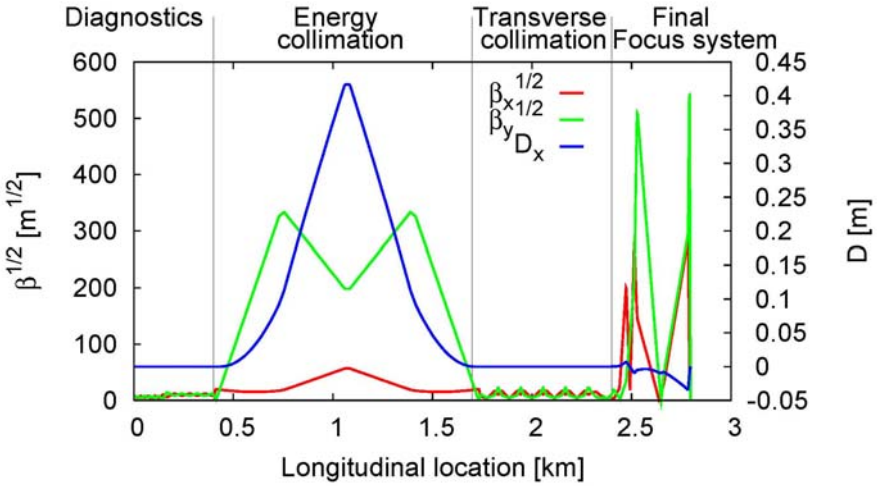

Figure 50: Optics of the CLIC beam delivery system [57]

6.4 Crab Crossing

With the horizontal crossing angle planned for ILC and CLIC the projected horizontal beam size would be many times the ideal intrinsic horizontal beam size, with an implied significant reduction in luminosity. The solution is to install "crab cavities," which are RF cavities operating in a transverse deflecting mode so that the bunches are tilted at the IP and collide effectively head-on (see Fig. 51). The bunch centroids still intersect at a crossing angle, which allows for easy separation and suppresses the multi-bunch kink instability.

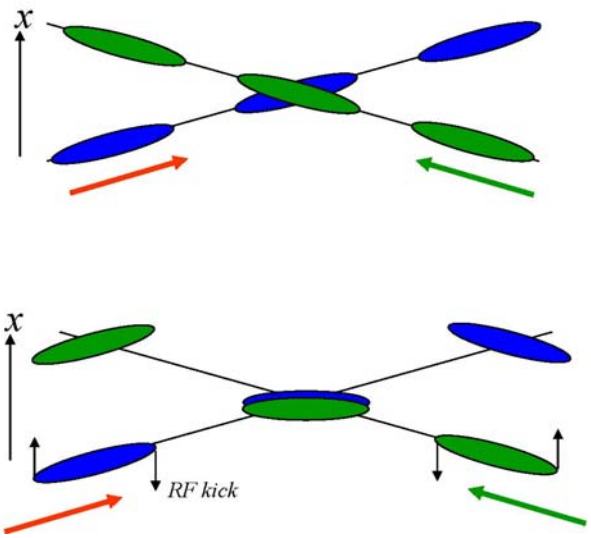

Figure 51: Schematic of conventional crossing (top) and crab crossing (bottom) [52].

6.5 Beam-Beam Effects

The beam-beam interaction in a linear collider is determined by the strong forces experienced during the collision process which result from the tiny (nm-size) transverse beam dimensions at the IP. Figure 52 illustrates the collision. Three prominent beam-beam processes are disruption, beamstrahlung, and pair creation.

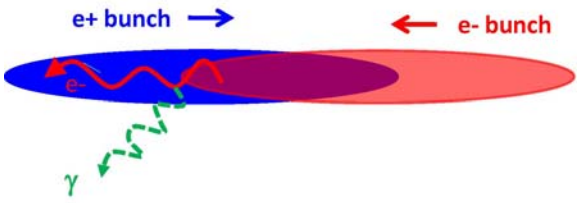

Figure 52: Collision between two bunches. In the strong field of the opposing positron bunch, electrons are “disrupted” and emit beamstrahlung photons.

The strength of focusing in the field of the opposite bunch is characterized by the disruption parameter [58]

$$D_{x,y} = \frac{\sigma_z}{\text{"focal length"}} = \frac{2r_e N_b \sigma_z}{\gamma \sigma_{x,y}\left(\sigma_x + \sigma_y\right)}$$

The number of oscillations undergone by a particle close to the beam axis during the collision process is approximately equal to $\sqrt{\sqrt{3}D}/(2\pi)$ [58]. The disruption parameter is closely linked to the “kink” instability which occurs for large values of $D_{x,y}$. The synchrotron radiation in the field of the opposite bunch is called “beamstrahlung”. Another important parameters is Y, the average value of which can be expressed as [58]

$$\mathrm{Y} \approx \frac{5}{6}\frac{N r_e^2 \gamma}{\alpha\sigma_z\left(\sigma_x+\sigma_y\right)}.$$

If Y~1 a significant number of beamstrahlung photons convert into e^+e^- pairs in the strong electromagnetic field of the two beams. The number of photons emitted per primary beam electron (or positron) [58]

$$N_\gamma \approx \frac{5}{2}\frac{\alpha\sigma_z}{\gamma\lambda\!\!\!^{-}_e}\mathrm{Y}\left[\frac{1}{\left(1+\mathrm{Y}^{2/3}\right)^{1/2}}\right] \approx 2\frac{\alpha r_e N_b}{\sigma_x+\sigma_y}$$

is directly linked to the luminosity energy spectrum and in particular to the fraction of luminosity at nominal energy [59]

$$\frac{\Delta L}{L} \approx \frac{1}{N_\gamma^2}\left(1-e^{-N_\gamma}\right)^2$$

A favorable luminosity spectrum requires N_γ~1, and all future linear collider designs achieve this while maintaining a high luminosity by colliding flat beams, with $\sigma_x >> \sigma_y$.
If the "Upsilon" parameter is much less than 1, Y equals two thirds of the ratio of photon energy to beam energy. When Upsilon acquires values of about ~1 or larger, the classical regime of synchrotron radiation is no longer applicable, and the quantum synchrotron-radiation formulae of Sokolov-Ternov should be used [52,58]. In the quantum regime, the synchrotron-radiation spectrum changes its shape and features a sharp cutoff due to the fact that the photons emitted cannot have an energy higher than the initial particle energy.

Table 9 compares beam-beam parameters for ILC and CLIC, the latter at both 500 GeV and 3 TeV centre-off-mass energy. The disruption is highest for ILC due to the long bunch length and high bunch charge. The high disruption could lead to a kink instability, but it may also helps to desensitize the collision against an initial transvere offset between the two beams. The Y parameter increases steeply with energy, lying deeply inside the quantum region at 3 TeV, resulting in an abundant creation of "coherent pairs". However, the CLIC design still succeeds in keeping N_γ reasonably small, close to a value of 2, even at 3 TeV.

Table 9: Beam-beam parameters for ILC at 500 GeV and CLIC at 500 GeV and 3 TeV centre-off-mass energy.

	ILC	**CLIC 500 GeV**	**CLIC 3 TeV**
D_y	18.3	11.7	7.4
Y	0.05	0.21	4.95
N_γ	1.3	1.3	2.2

Incoherent pair production is always present. Here,beamstrahlung photons, particles of beams or virtual photons interact, to create e+e- pairs via one of three different scattering processes: $\gamma\gamma \rightarrow e^+e^-$ (Breit-Wheeler process), $e^\pm\gamma \rightarrow e^\pm e^+e^-$ (Bethe-Heitler process), and $ee \rightarrow eee^+e^-$ (Landau-Lishitz process). In addition, for large Y values, coherent pairs are generated by photons in the field of the opposite bunch, which is called the coherent pair production.

Figure 52 presents the differential luminosity spectrum for CLIC at four different centre-of-mass energies [60].

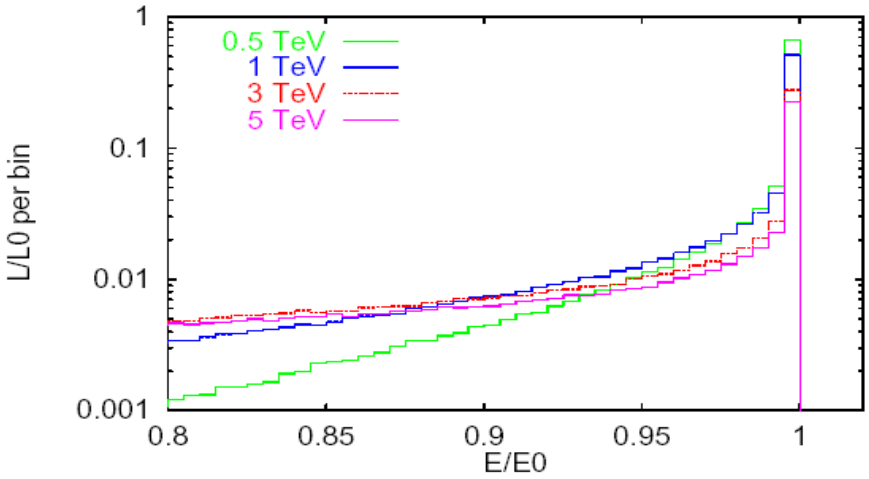

Figure 52: Simulated differential luminosity spectrum as a function of normalized energy for CLIC at four different centre-of-mass energies [60].

6.6 Linear-Collider Detectors and Physics

There presently are three detector collaborations for the ILC (called the "ILD", "SiD", and "the 4th") and one for CLIC. Detector performance simulations look at events like t-tbar production Higgs production, or WW scattering [61].

7. ILC Overview

Figure 53 shows the machine layout of the International Linear Collider (ILC) [3,62]. Various components can be seen. The ILC is designed for an energy of 200-500 GeV in the centre-of-mass and a luminosity of 2×10^{34} $cm^{-2}s^{-1}$. The length of the two superconducting linacs and the total size of the ILC site of 31.5 km are based on an accelerating gradient of 31.5 MV/m at 1.3 GHz RF frequency.

Figure 55 displays the flow of positrons and electrons through the ILC beam-line system. In particular the tight coupling between electron acceleration and positron production can be noticed. The ILC SC linac consists of structures with either 8 or 9-cell cavities.

Two 4.5 to 5.5 m diameter ILC tunnels are spaced by ~7 m, as sketched in Figure 55. The baseline RF power distribution system for ILC is illustrated in Fig. 56. An alternative RF powering configuration, known as "cluster klystron," is also under consideration, where the RF power of 350 MW from 2x35 klystrons would be "piped" into the accelerator tunnel every 2.5 km through 0.5-m diameter over-moded circular waveguides, and the service tunnel eliminated. Electrical and cooling systems would be simplified. Concerns relate to the power handling, and to the low-level RF control coarseness.

The RF technology parameters required for the ILC are summarized in Table 10.

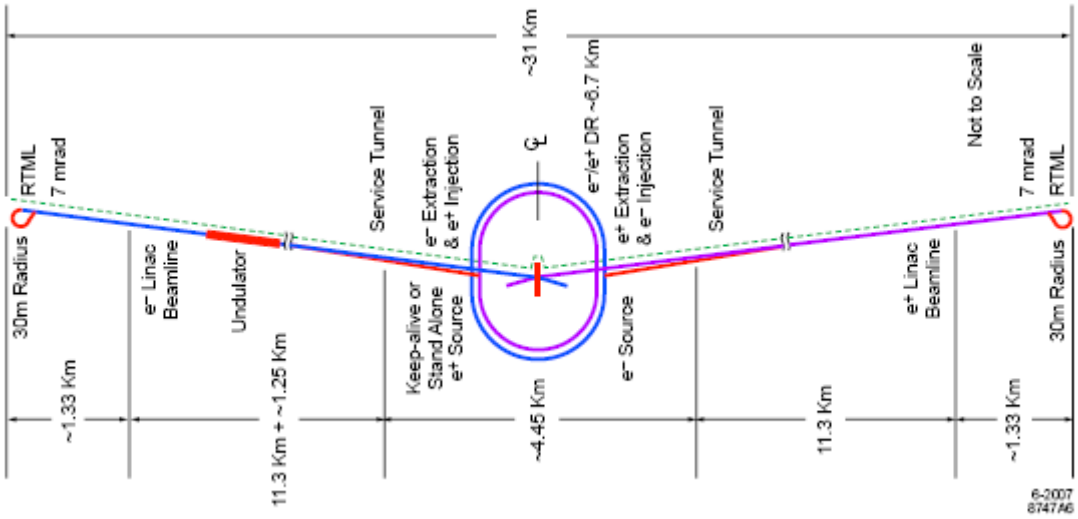

Figure 53: ILC machine layout [62].

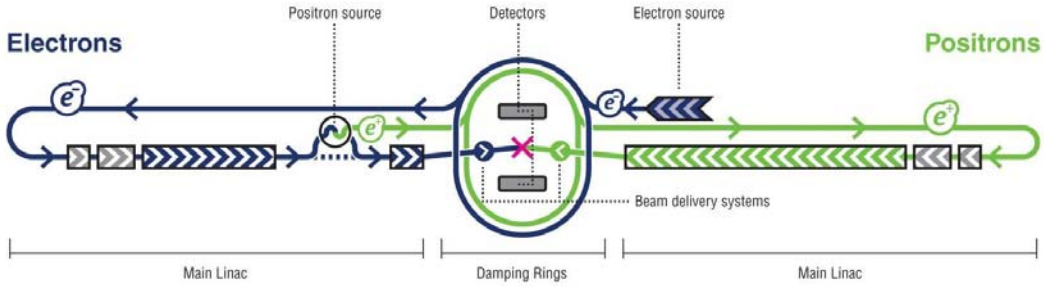

Figure 54:Electron and positron flow through the ILC systems [62].

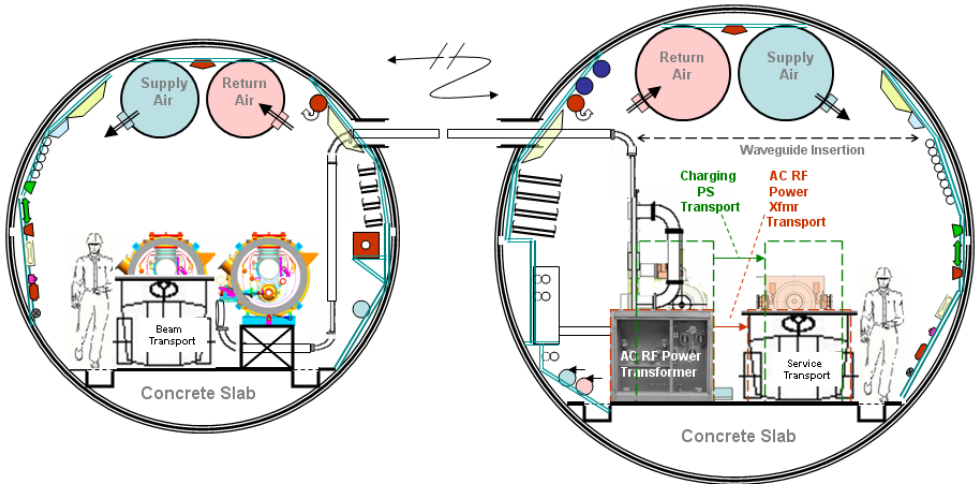

Figure 55: ILC baseline tunnel layout: every 12 metres the accelerator tunnel (left) and service tunnel (right) are connected by penetrations [62].

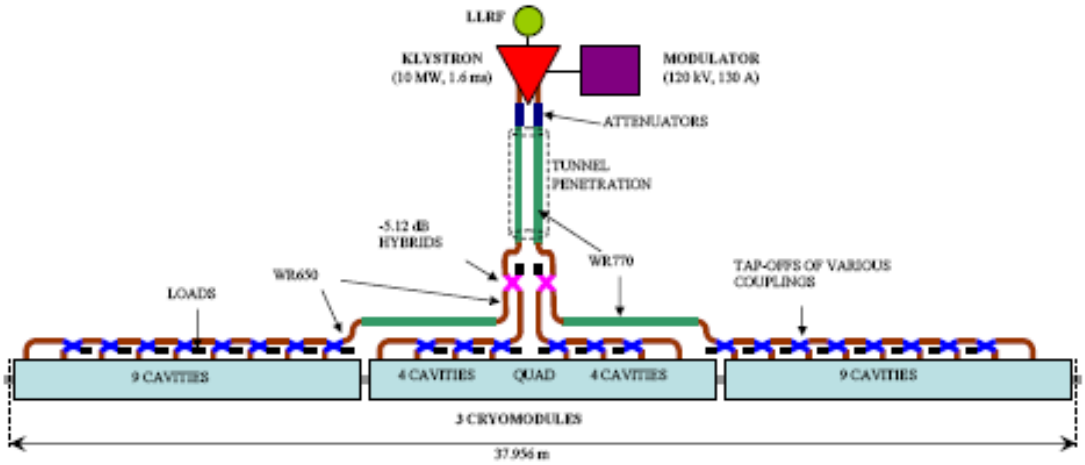

Figure 56: Layout of the ILC RF power distribution system [62]. One klystron feeds 26 cavities.

Table 10: Parameters of the required ILC RF technology

Parameter	Value
C.M. Energy	500 GeV
Peak luminosity	$2x10^{34}$ $cm^{-2}s^{-1}$
Beam Rep. rate	5 Hz
Pulse time duration	1 ms
Average beam current	9 mA (in pulse)
Av. field gradient	31.5 MV/m
# 9-cell cavities	14,560
# cryomodules	1,680
# RF units	560

Many outstanding ILC issues are addressed through three superconducting-RF test facilities: The "NML" facility at Fermilab (near Chicago) is under construction, with first beam in 2010. "TTF/FLASH" at DESY (Hamburg) is already operating an ILC-like beam at 1 GeV energy. "STF" at KEK (Tsukuba) is being constructed for first beam in 2011. All three facilities represent ILC RF unit tests. Other ILC R&D is also ongoing in several test facilities [3]: beam tests at FLASH (DESY), at ATF2 (KEK) for fast kicker performance, and final focus design tests and at CesrTA for electron-cloud mitigation.

The ILC time line defined by the "Global Design Effort" (GDE) is presented in Fig. 57.

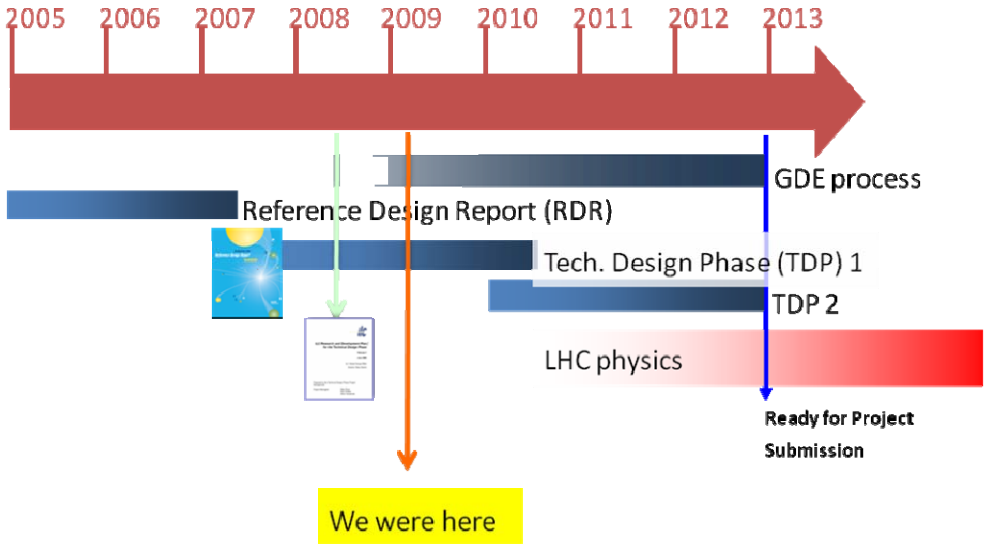

Figure 57: The ILC time line [3].

8. The CLIC Two-Beam Scheme

CLIC aims for collision energies up to 5 TeV in the centre-off-mass. The nominal design is for 3 TeV. Individual RF power sources are not an option for 1.5-TeV linacs. Instead the CLIC design is based on a novel two-beam acceleration scheme, where a drive beam supplies the RF power. The drive beam is characterized by a 12 GHz bunch structure, low energy (2.4 GeV - 240 MeV), and high current (100 A).

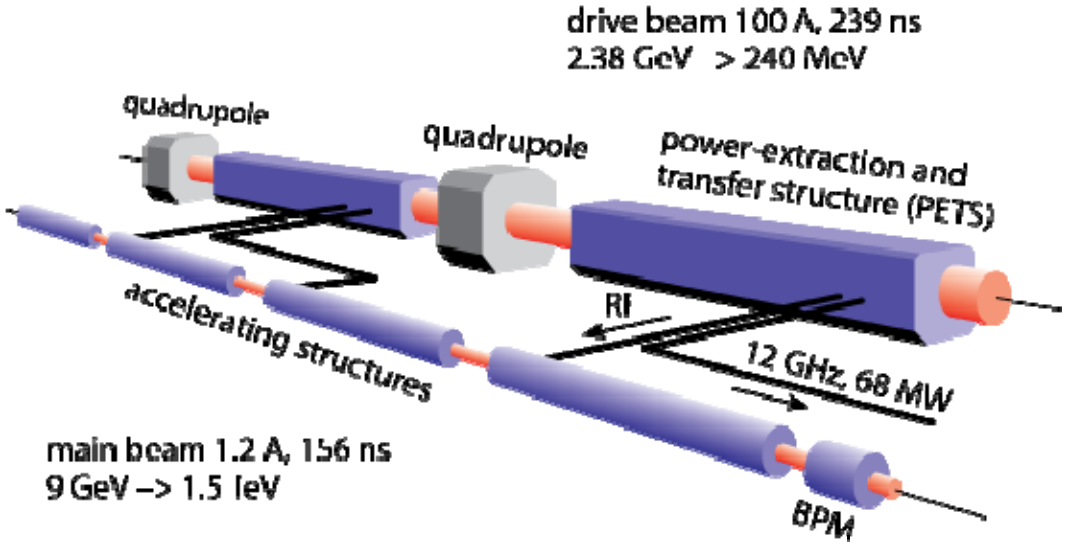

Figure 58: Schematic of the CLIC two-beam acceleration scheme, where an intense low-energy drive beam is decelerated, the liberated energy extracted and fed into the accelerating structures of the main beam running in parallel [3].

The drive beam for one linac consists of 24 trains of 2904 bunches with a bunch charge of 8.4 nC and bunches spaced by 83 ps (12 GHz). The length of a train is 240 ns,, the current in a train 100 A, and successive trains are separated by 5.8 μs. The 24 trains extend over 139 μs. Each drive-beam bunch train feeds a different 876-m long decelerator section.

One CLIC challenge is the generation of the drive beam. This is done by accelerating long bunch train with low bunch repetition rate (500 MHz) at a low RF frequency (1 GHz), where klystrons are available. Bunches are interleaved between each other to generate short (240 ns) trains with a high bunch repetition rate (12 GHz). The drive-beam generation complex, including delay loop and combiner rings, used for the interleaving, is illustrated in Fig. 59. The full CLIC complex for 3 TeV is shown in Fig. 60, where the drive beam complex occupies the upper half of the picture and the main beam components the lower part. Figure 61 presents details of the CLIC acceleration and the tunnel cross section. An important feature of CLIC is that there are no active elements inside or along the tunnel.

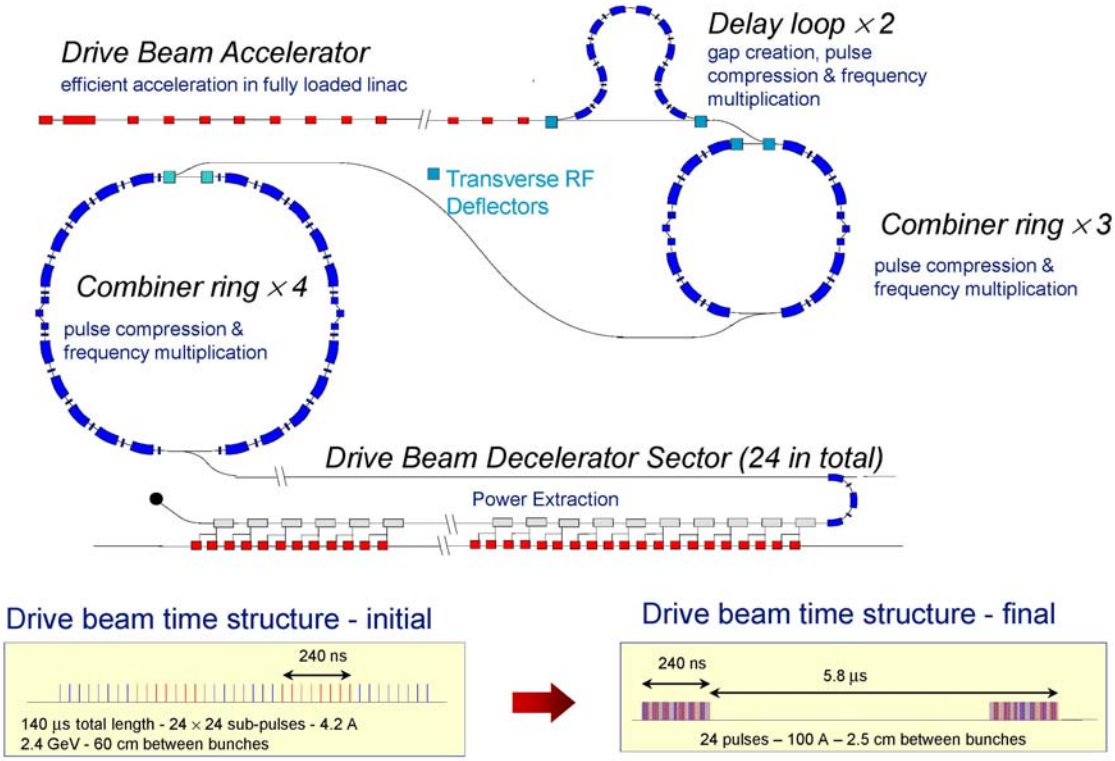

Figure 59: CLIC drive-beam generation complex.

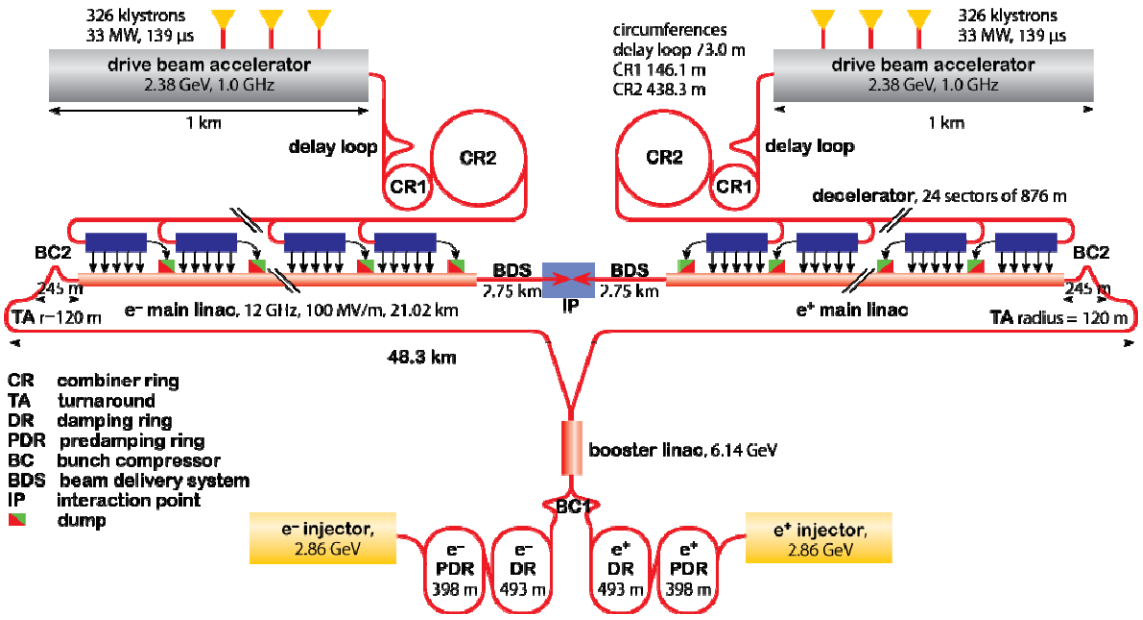

Figure 60: The full CLIC complex for collisions at 3-TeV center-of-mass energy.

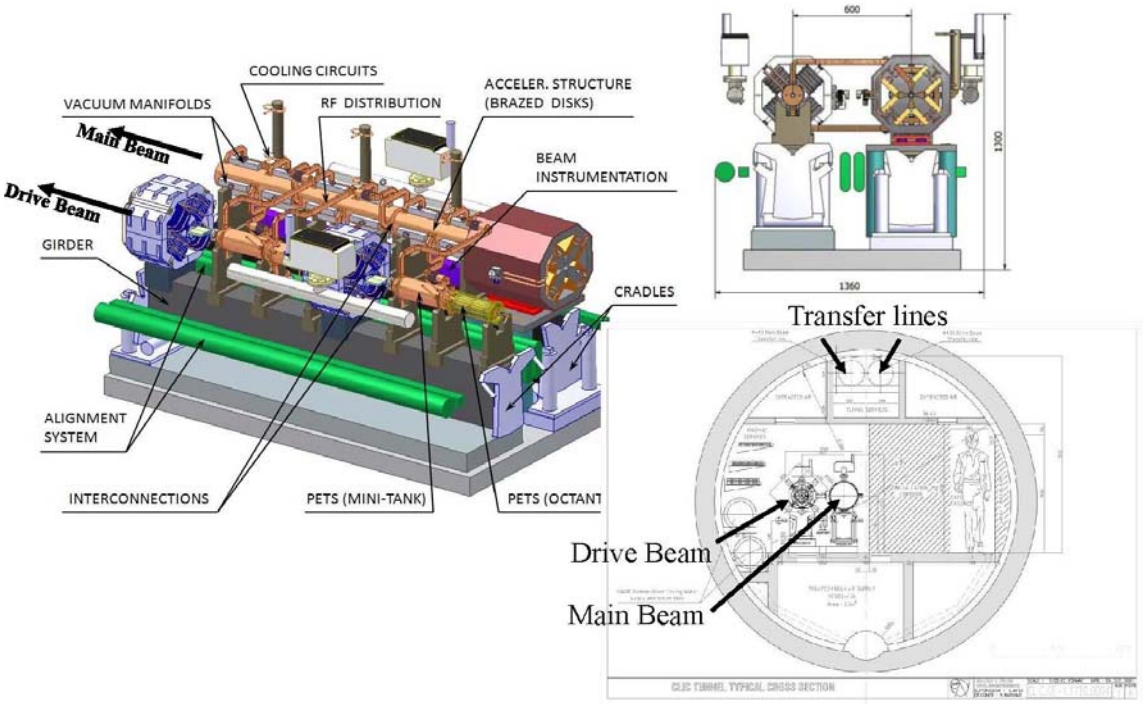

Figure 61: CLIC acceleration module and tunnel cross section (Germana Riddone) [3].

The objective for the CLIC accelerating structures is to withstand an accelerating gradient of 100 MV/m without damage, at a breakdown rate of less than 10^{-7}, and with a strong damping of the higher-order modes (to prevent multi-bunch beam breakup in the linac). CLIC accelerating structures are being developed by a CERN-KEK-SLAC collaboration. Several prototype accelerating structures designed at CERN and built & tested at KEK and at SLAC

have reached the nominal performance, i.e. and acceleration field of 100 MV/m with a breakdown rate below 10^{-7} (Fig. 16).

The Power Extraction and Transfer Structures (PETs) are a specific development for CLIC. Each CLIC linac will have about 36000 such PETs. The design requires a PET to extract 136 MW RF power over 240 ns, feeding 2 accelerating structures. In the "CTF3" test facility at CERN up to 45 MW peak power has been achieved so far (using a 3 A beam in recirculation), and at SLAC 125 MW over 266 ns, as well as 180 MW over 133 ns.

To achieve the CLIC design luminosity of $2x10^{34}$ $cm^{-2}s^{-1}$, the beam size at the interaction point must be small σ_x = 40 nm, σ_y = 1 nm, and the total site AC power becomes 392 MW. CLIC design issues comprise the generation of small emittance beams, emittance preservation. alignment and vibration control, amd final focus (or beam delivery system) . The CLIC jitter tolerances of Table 11 look ambitious. However, a proof-of-principle study already demonstrated the stability to better than 0.5 nm above 4 Hz in the vertical plane [63].

Table 11: Transverse vibration jitter tolerances for the CLIC final-focus and main-linac quadrupoles in the critical frequency ranges above 1 or 4 Hz, where the respective fast orbit feedback is not active.

	final-focus quadrupoles	main beam quadrupoles
vertical	~0.1 nm (> 4 Hz)	~1 nm (> 1 Hz)
horizontal	2 nm (> 4 Hz)	5 nm (> 1 Hz)

CLIC can be constructed and commissioned in phase or stages. Figure 62 sketches four different phases in energy and luminosity. For comparison two ILC working points are also indicated.

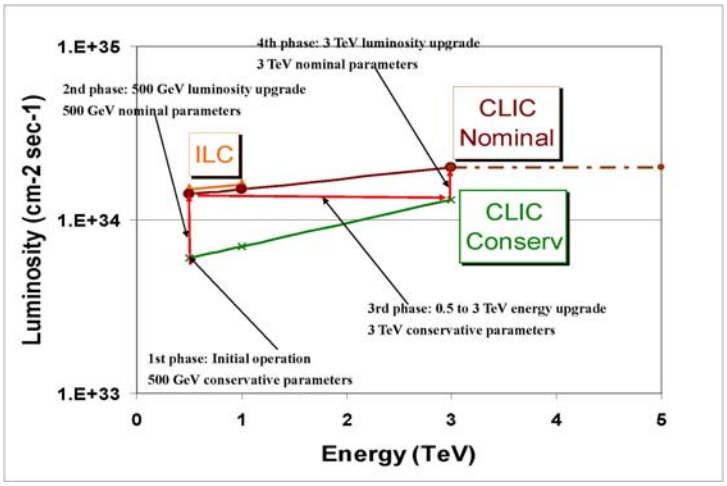

Figure 62: CLIC staging scenario in energy-luminosity space [3,64].

Figure 63 compares transverse IP beam sizes for CLIC with those of other facilities, planned or operated. Table 12 summarizes conservative and nominal CLIC main parameters for two different beam energies.

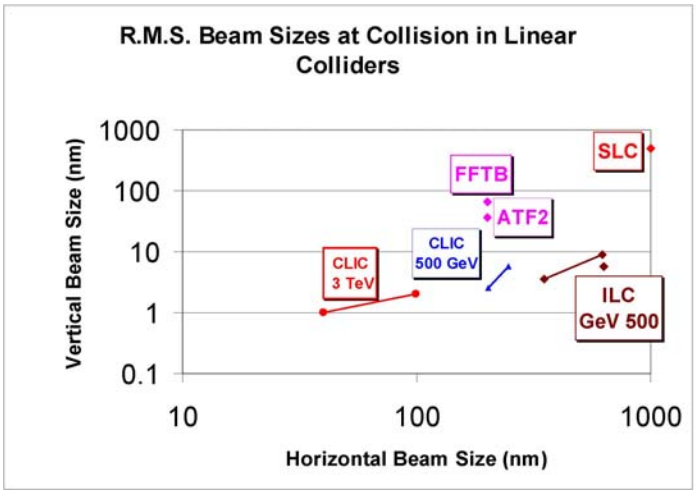

Figure 63: Beam size in collision for CLIC compared with several other projects [3].

Table 12: CLIC main parameters at 500-GeV and 3-TeV centre-of-mass energy [3,64].

Center-of-mass energy	CLIC 500 G		CLIC 3 TeV	
Beam parameters	Conservative	Nominal	Conservative	Nominal
Accelerating structure	502		G	
Total (Peak 1%) luminosity	$0.9(0.6)\cdot10^{34}$	$2.3(1.4)\cdot10^{34}$	$1.5(0.73)\cdot10^{34}$	$5.9(2.0)\cdot10^{34}$
Repetition rate (Hz)	50			
Loaded accel. gradient MV/m	80		100	
Main linac RF frequency GHz	12			
Bunch charge10^9	6.8		3.72	
Bunch separation (ns)	0.5			
Beam pulse duration (ns)	177		156	
Beam power/beam (MWatts)	4.9		14	
Hor./vert. norm. emitt ($10^{-6}/10^{-9}$)	3/40	2.4/25	2.4/20	0.66/20
Hor/Vert FF focusing (mm)	10/0.4	8 / 0.1	8 / 0.3	4 / 0.07
Hor./vert. IP beam size (nm)	248 / 5.7	202 / 2.3	83 / 2.0	40 / 1.0
Hadronic events/crossing at IP	0.07	0.19	0.57	2.7
Coherent pairs at IP	10	100	$5\ 10^7$	$3.8\ 10^8$
BDS length (km)	1.87		2.75	
Total site length km	13.0		48.3	
Wall plug to beam transfert eff	7.5%		6.8%	
Total power consumption MW	129.4		415	

The goal of the CLIC Test Facility no. 3 ("CTF-3") is to provide answers to CLIC specific issues and to support the CLIC Conceptual Design Report to be written in 2010. More precisely, its main two missions are (1) to prove the CLIC RF power source scheme as regards bunch manipulations, beam stability, and drive-beam generation, 12 GHz extraction, as well as to demonstrate a "relevant" linac sub-unit including acceleration of a test beam, and (2) to provide RF power for the validation of CLIC components, such as accelerating structures, RF distribution, and the PETS. CTF-3 is a scaled down from CLIC, as is illustrated in Table 13.

Table 13: Comparison of key parameters for CTF-3 and the real CLIC drive-beam complex [3].

	CLIC	CTF3
drive Beam energy	2.4 GeV	150 MeV
compression / frequency multiplication	24 (Delay Loop +2 Combiner Rings)	8 (Delay Loop + 1 Combiner Ring)
Drive Beam current	4.2 A*24 →101 A	3.5 A * 8→ 28 A
RF Frequency	1 GHz	3 GHz
train length in linac	139 ms	1.5 ms
energy extraction	90 %	~ 50 %

While the basic concept of two-beam acceleration had already been proven in a previous test facility, CTF-2, CTF-3 has so far demonstrated the operation of the drive-beam linac in cw mode, the functioning of the delay loop, and a four-fold current increase in the combiner ring. Some other, more general CLIC feasibility issues are addressed in international facilities, like ATF, ATF2, CESR-TA, LCLS, SLS, X-FEL, etc., through the worldwide CLIC&CTF-3 collaboration that involves 33 institutes from 18 countries [3]. A success-oriented CLIC schedule is depicted in Fig. 64.

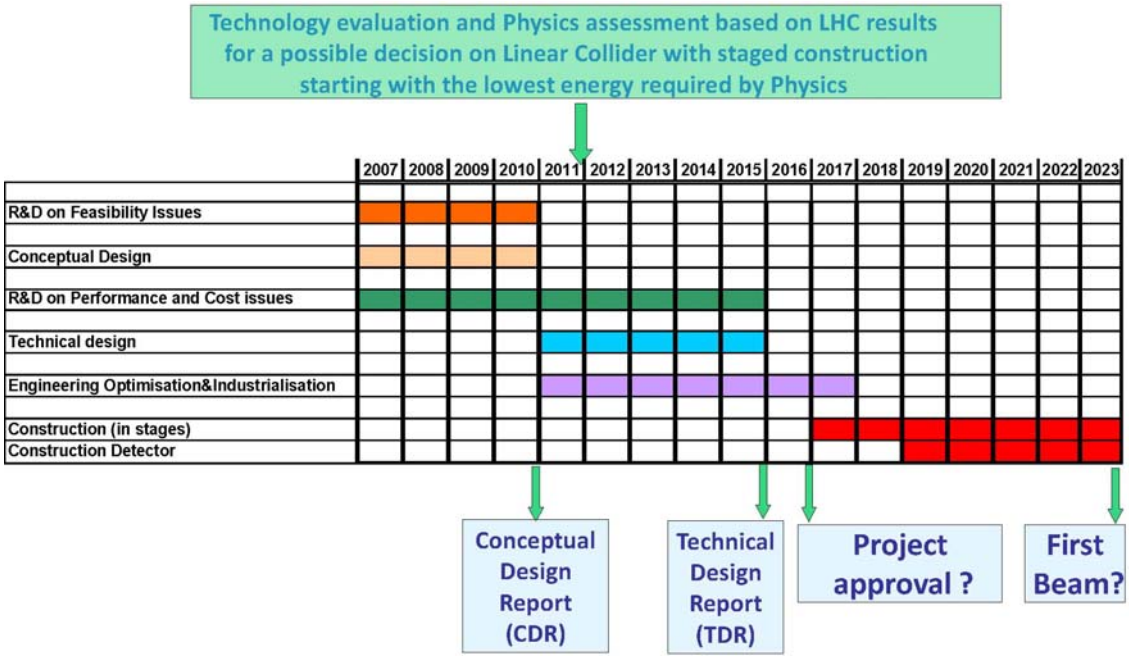

Figure 64: Tentative long-term CLIC scenario – the shortest, success-oriented, technically limited schedule [3].

9. Contrasting Parameters for ILC and CLIC

The ILC is based on a superconducting linac and its design centre-off-mass collision energy is 500 GeV. CLIC uses normal-conducting copper RF, with 3-TeV design energy. CLIC can also be operated at 500 GeV, e.g. in a first phase (see Fig. 62). The main parameters of CLIC and ILC are compared in Table 14. The peak luminosity for the two 500-GeV designs is almost the same, while the beam pulse duration, accelerating gradient, and total power consumption are quite different.

The ILC design accelerating gradient is 31.5 MV/m, compared with 100 MV/m for CLIC, translating into more than 3 times shorter length of CLIC for the same energy The RF peak power for ILC is 0.37 MW/m, with a pulse length of 1.6 ms at 5 Hz repetition rate. For CLIC the RF peak power amounts to the much higher value of 275 MW/m, but only over 240 ns at 50 Hz. Combining these numbers, the average RF power turns out to be rather similar: 2.9 kW/m for ILC and 3.6 kW/m for CLIC. The total collider length is 31 km at 500 GeV for the ILC, and 48.4 km at 3 TeV for CLIC. The ILC site power is 230 MW at 500 GeV, the CLIC site power 392 MW at 3 TeV (and 130 MW at 500 GeV).

The main beam structure differs markedly between the two design concepts. ILC features 2625 bunches per pulse of 0.96 ms with a bunch population of $2\text{x}10^{10}$ electrons or positrons. A CLIC pulse is only 156 ns long, containing 312 bunches each with a population of $3.7\text{x}10^{9}$ electrons or positrons. The ILC bunch spacing of 369 ns is almost three orders of magnitude larger than the 0.5-ns CLIC bunch spacing.

Further differences between ILC and CLIC, in addition to those mentioned above, are compiled in Table 15.

The earlier TESLA design [66] corresponded to a “safe” machine. Cost saving needs might increase ILC risks. One example is the electron cloud. Figure 65 illustrates that the original TESLA parameters were below the electron–cloud threshold observed at SPS, CERN PS, APS, and the Tevatron, while the modified ILC damping ring parameters are above this threshold, in a region where KEKB has suffered from strong electron-cloud effects.

Table 14: CLIC and ILC parameters [61,65].

centre-of-mass energy	ILC 500 GeV	CLIC 500 GeV	CLIC 3 TeV
total (peak 1%) luminosity [10^{34} $cm^{-2}s^{-1}$]	2(1.5)	2.3 (1.4)	5.9 (2.0)
repetition rate [Hz]	5	50	
loaded accelerating gradient [MV/m]	32	80	100
main linac RF frequency [GHz]	1.3	12	
particles per bunch [10^9]	20	6.8	3.7
bunch separation [ns]	370	0.5	
beam pulse duration [ns]	950,000	177	156
beam power / beam [MW]	10.8	4.9	14
horizontal/vertical IP beam size [nm]	639, 5.7	200, 2.3	40, 1.0
#hadronic events / crossing at IP	0.12	0.2	2.7
incoherent pairs at IP [10^5]	1.0	1.7	3.0
crossing angle [mrad]	14	18.6	20
beam delivery system length / beam [km]	2.23	1.87	2.75
total site length [km]	31	13	48
total electrical power consumption [MW]	230	130	415

Table 15: Further differences between ILC and CLIC.

ILC	CLIC
large size of damping rings ~ 6 km	compact injector complex
must rely on undulator e+ source: - couples e- and e+ operation - risk to main beam - transient effects in DRs	tighter tolerances on magnet vibration, power supply ripple etc (lower emittance, larger wake fields) [but w/o cryostats]
ILC SC linac has ~20% better el.-power to beam power conversion efficiency, but ~2x more electrical power at same energy& luminosity	~3 times shorter length for same energy & lower construction cost per GeV
2-3 years more mature	higher energy reach
long pulses, large bunch separation, 5 Hz (detector, intrapulse feedbacks)	short pulses, short bunch spacing, 50 Hz (pulse-to-pulse feedback) & beam-beam effects at 3 TeV
2 times lower energy spread	

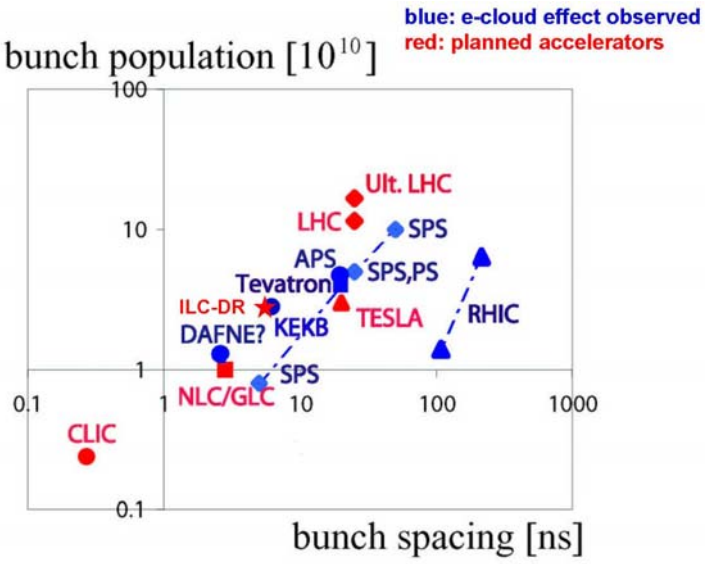

Figure 65: Bunch population above which electron-cloud effects are observed in various accelerations (blue) as a function of bunch spacing, and target design parameters of several future accelerators (red) [67].

That the "advantage of superconductors for linear-collider cavities [is] not at all that obvious…" [68] is illustrated by the fact that in 2003 only 1 of 4 linear-collider designs considered SC cavities. The traditional arguments against SC are low accelerating fields (strong physical limitation), and the high cost of cryogenic equipment. The TESLA and ILC R&D have made great progress on both issues and enabled numerous novel applications of SC RF linac

technology hitherto unthinkable (e.g. for high-intensity proton drivers, or electron energy-recovery linacs). However, as far as high-energy linear colliders are concerned, the above two arguments may still be valid today.

10. Outlook – LHeC as Intermediate Step?

A possible intermediate step forward, prior to constructing a full-blown ILC or CLIC, could be a linac for a Large Hadron electron Collider (LHeC) [69,70], as illustrated in Figs. 66 and 67. The electron linac of the LHeC could be either superconducting, profiting from ILC technology, with electron bunches separated by multiples of the LHC bunch spacing [69] or be based on the CLIC concept. In the latter case, one or two CLIC drive beam units would suffice to reach an electron energy of 70-140 GeV, and the highest luminosity would be achieved by colliding about 100-ns long CLIC-type bunch trains with proton super-bunches in the LHC [71].

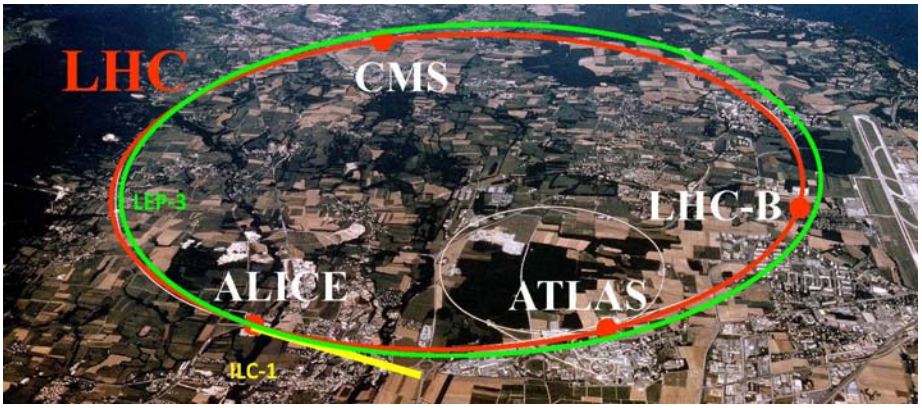

Figure 66: A linac-ring Large Hadron electron Collider (LHeC) based on the LHC could consist of a electron large storage ring in the LHC tunnel ("LEP-3") or be a linac, either based on CLIC technology or possibly an ILC-type SC linac with energy recovery ("ILC-1") [69].

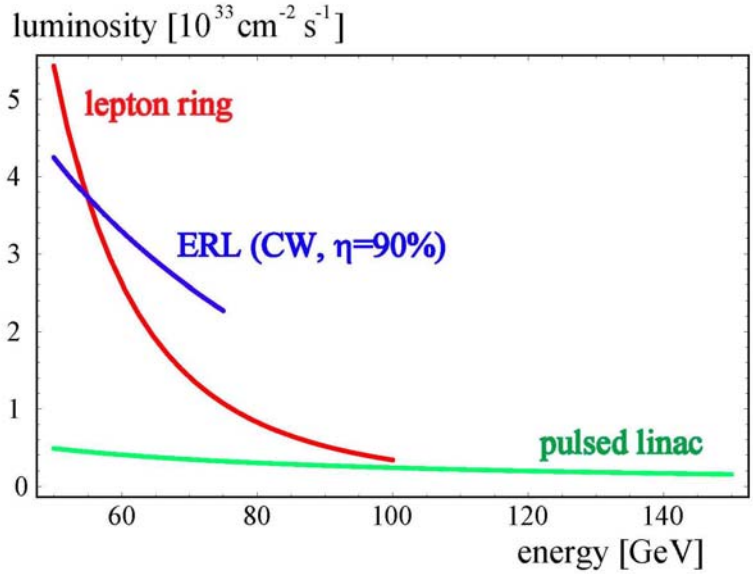

Figure 67: Luminosity versus electron beam energy for an LHeC based on a lepton ring, a pulsed SC linac, or a cw SC linac with energy recovery, at a wall-plug power of 100 MW [69].

Acknowledgements

I would like to thank Andre Sopczak and Daniel Schulte for providing the great opportunity to participate in this UK linear-collider summer school, Ted Wilson for valuable advice while preparing the lecture, the students and co-lecturers for many interesting and pleasant discussions, and several colleagues – including Erik Adli, Ralph Assmann, Jean-Pierre Delahaye, Günther Geschonke, Alexej Grudiev, Erk Jensen, Masao Kuriki, Yannis Papaphilippou, Louis Rinolfi, Daniel Schulte, and Rogelio Tomas – for their numerous helpful comments on the topics of this lecture and on the manuscript.

References

[1] A. Mosnier, *Radiofrequency Accelerators*, HEEAUP Workshop Paris 2005

[2] E. Jensen, *RF*, CERN Accelerator School, Divonne 2009

[3] G. Geschonke, *The next energy-frontier accelerator - a linear e+e- collider?*, EPS HEP2009 Conference, Krakow, 2009

[4] T. Higo, *LINAC*, ILC School, Chicago, 2008

[5] E. Adli, *Particle Colliders – The Next Generation*, 2009

[6] A. Eide, *Electrical power of ring-linac options for LHeC (T4 Report)*, EPFL Lausanne, June 2008

[7] U. Amaldi, private communication, 2009

[8] N. Phinney et al, *ILC Reference Design Report*, Vol. 3, 2007

[9] F. Tecker et al, *CLIC Parameter List 3 TeV*, 11.10.2007 http://clic-meeting.web.cern.ch/clic-meeting/clictable2007.html

[10] K. Oide, *Synchrotron Radiation Limit on the Focusing of Electron Beams*, Phys. Rev. Lett. 61: 1713-1715, 1988

[11] L. Lilje, *Global Design Effort. 1. Cavity Gradient R&D*, TILC'09 AAP, Tsukuba, April 2009

[12] A. Grudiev, *Update on Structure Optimization Procedure, Input and Results. CLIC Reference Structure*, Report to CLIC-ACE, 16.01.2008

[13] A. Grudiev, W. Wuensch, *A New Local Field Quantity Describing the High Gradient Limit of Accelerating Structures*, LINAC08 Victoria, 2008

[14] M. Kuriki, *Electron Source for Linear Colliders*, 2nd ILC School Erice, 2007

[15] M. Kuriki, private communication, July 2009

[16] L. Rinolfi, private communications, 2009

[17] M. Kuriki, *Positron Source for Linear Colliders*, 2nd ILC School Erice, 2007

[18] V.E. Balakin, A.A. Mikhailichenko, *Conversion system for Obtaining Highly Polarized Electrons and Positrons*, INP-79-85, 1979

[19] L. Rinolfi, *Present Roadmap for the CLIC Positron Sources*, POSIPOL2009 Lyon

[20] L. Rinolfi, F. Antoniou, H.-H. Braun, Y. Papaphilippou, D. Schulte, A. Vivoli, F. Zimmermann, E.V. Bulyak, P. Gladkikh, R. Chehab, J.A. Clarke, O. Dadoun, P. Lepercq, R. Roux, A. Variola, Z.F. Zomer, W. Gai, W. Liu, T. Kamitani, T. Omori, J. Urakawa, M. Kurik, I. Pogorelsky, V. Yakimenko, T. Takahashi, *The CLIC Positron Source Based on Compton Schemes*, PAC'09 Vancouver, 2009

[21] F. Zimmermann Y. Papaphilippou, L. Rinolfi, A. Vivoli, V. Yakimenko, M. Kuriki, R. Chehab, T. Omori, J. Urakawa, A. Variola, F. Antoniou, *Stacking Simulations for Compton Positron Sources of Future Linear* Colliders, PAC'09 Vancouver, 2009

[22] T. Omori, L. Rinolfi, F. Zimmermann, discussion at ILC'09 in Tsukuba, April 2009

[23] J. Clarke, *The Positron Source*, TILC'09 AAP Review, Tsukuba, April 2009

[24] B. Lengeler, RWTH Aachen, lecture on coherence

[25] J. Schwinger, *On the Classical Radiation of Accelerated Electrons*, Physical Review 75, 12 (1949).

[26] G. Margaritondo, *A Primer in Synchrotron Radiation: Everything You Wanted to Know about SEX (Synchrotron Emission of X-rays) but Were Afraid to Ask*, J. Synchrotron Radiation 2, 148 (1995).

[27] H. Wiedemann, *Synchrotron Radiation in Storage Rings*, Section 3.1.4 in Handbook of Accelerator Physics and Engineering, A. Chao and M. Tigner (eds.), World Scientfic 1998

[28] H. Wiedemann, *Electron Storage Ring*, Turkish National Accelerator and Detector Summer School, Bodrum, Turkey, 2007

[29] M. Sands, *The Physics of Electron Storage Rings – An Introduction*, SLAC-121, 1970

[30] E. Levichev, P. Piminov, D. Shatilov, *Nonlinear Beam Dynamics with Strong Damping and Space Charge in the CLIC Damping Ring*, Proc. PAC'09 Vancouver, 2009

[31] K. Robinson, *Radiation Effects in Circular Electron Accelerators*, Phys. Rev. 111, 373 (1958).

[32] Y. Papaphilippou, *CLIC Damping Rings Overview*, CLIC Meeting, CERN, 5 September 2008

[33] Z. T. Zhao, *Commissioning of New Synchrotron Radiation Facilities*, Proc. PAC'07 Albuquerque, 2007

[34] R. Siemann, *Accelerator Physics – Wakefields, Impedance, Collective Effects and Instabilities*, SLAC SLUO Lectures, 1998

[35] T. Weiland, *TBCI and URMEL--New Computer Codes for Wake Field and Cavity Mode Calculations*, Particle Accelerator Conf., Santa Fe, New Mexico, Mar 21-23, 1983, IEEE Trans.Nucl.Sci.30:2489-2491, 1983

[36] K. Bane, *Landau Damping in the SLAC Linac*, Particle Accelerator Conf., Vancouver, B.C., Canada, May 13-16, 1985

[37] V.E. Balakin, A.V. Novokhatsky, V.P. Smirnov, *VLEPP: Transverse Beam Dynamics*, 12th Int. Conf. on High Energy Accelerators, Batavia, IL, 11-16 Aug 1983

[38] W. Schnell, *Microwave Quadrupoles for Linear Colliders*, CERN-LEP-RF/87-24, CLIC Note 34, 1987

[39] F. Zimmermann, *Review of Single Bunch Instabilities Driven by an Electron Cloud*, 31st ICFA Beam Dynamics Workshop: Electron Cloud Effects (ECLOUD04), Napa, California, 19-23 April 2004, Phys.Rev.ST Accel.Beams 7:124801, 2004

[40] C.L. O'Connell, *Plasma Production Via Field Ionization*, PhD Thesis, Stanford U, 2005

[41] O. Gröbner, R.S. Calder, *Beam Induced Gas Desorption in the CERN Intersecting Storage Rings*, IEEE PAC'73San Francisco, 1973

[42] R. Cimino, I.R. Collins, M.A. Furman, M. Pivi, F. Ruggiero, G. Rumolo, F. Zimmermann, *Can Low-Energy Electrons Affect High-Energy Physics Accelerators?*, Phys.Rev.Lett.93:014801, 2004

[43] K. Ohmi, F. Zimmermann, *Head-Tail Instability Caused by Electron Cloud in Positron Storage Rings*, Phys.Rev.Lett.85:3821-3824, 2000

[44] F. Zimmermann, W. Bruns, D. Schulte, *Ion Effects in the Damping Rings of ILC and CLIC*, European Particle Accelerator Conference (EPAC 06), Edinburgh, Scotland, 26-30 Jun 2006

[45] F. Zimmermann, P. Krejcik, M. Minty, D. Pritzkau, T. Raubenheimer, M. Ross, M. Woodley, *Ion Effects in the SLC Electron Damping Ring under Exceptionally Poor Vacuum Conditions*, International Workshop on Multibunch Instabilities in Future Electron and Positron Accelerators, Tsukuba, Japan, 15-18 Jul 1997, KEK Proc. 97-17, 1997

[46] T.O. Raubenheimer, F. Zimmermann, *A Fast Beam-Ion Instability in Linear Accelerators and Storage Rings*, Phys.Rev.E52:5487-5497, 1995

[47] G.V. Stupakov, A Fast Beam-Ion Instability, International Workshop on Collective Effects and Impedances for B-Factories (CEIBA95), Tsukuba, Japan, 12-17 June 1995, KEK Proceedings 96-6, 1996

[48] J. Irwin, *The Application of Lie algebra techniques to beam transport design*, Nucl. Instrum. Meth. A298, 460-472, 1990

[49] R. Tomas et al, *ATF2 Ultra-Low IP Betas Proposal*, PAC'09 Vancouver, 2009

[50] K. Brown, *A Second Order Magnetic Optical Achromat*, SLAC-PUB-2257, 1979

[51] K. Brown, R. Servranckx, *Applications of the Second Order Achromat Concept to the Design of Particle Accelerators*, Particle Accelerator Conf., Vancouver, Canada, IEEE Trans.Nucl.Sci.32:2288,1985 (No.5)

[52] A. Seryi, *Beam Delivery & Beam-Beam*, ILC School, Erice, 2007

[53] F. Zimmermann, *Tutorial on Linear Colliders*, JAS'2000: High Quality Beams, Petersburg - Moscow, Russia, 1-7 Jul 2000, Published in High quality beams* 494-551

[54] F. Zimmermann, *New Final Focus Concepts at 5-TeV and Beyond*, Advanced Accelerator Concepts Workshop, Baltimore, MD, 1988, AIP Conf.Proc.472:103-141,1999

[55] P. Raimondi, A. Seryi, *A Novel Final Focus Design for Future Linear Colliders*, Phys.Rev.Lett.86: 3779-3782, 2001

[56] R. Assmann, private communication

[57] R. Tomás, B. Dalena, J. Resta-López, G. Rumolo, D. Schulte, D. Angal-Kalinin, F. Jackson, B. Bolzon, L. Brunetti, N. Geffroy, A. Jeremie, K.P. Schuler, A. Seryi, *Status of the CLIC Beam Delivery System*, Proc. PAC"09 Vancouver, 2009

[58] P. Chen, K. Yokoya, *Beam-Beam Phenomena in Linear Colliders*, Lecture at 1990 US-CERN School on Particle Accelerators, Hilton Head Island, South Carolina, 7-14 November 1990.

[59] The NLC Design Group (C. Adolphsen et al), *Zeroth-Order Design Report for the Next Linear Collider*, SLAC-R-474, 1996

[60] D. Schulte, *High Energy Beam-Beam Effects in CLIC*, Proc. IEEE Particle Accelerator Conference (PAC 99), New York, 29 March - 2 April 1999

[61] L. Linssen, *News from CLIC*, Posipol2009 workshop, Lyon, 2009

[62] J. Brau et al, *International Linear Collider Reference Design Report. 1: Executive Summary. 2: Physics at the ILC. 3: Accelerator. 4: Detectors*, ILC-REPORT-2007-001, AAI-PUB-2007-002, BNL-79150-2007, CERN-2007-006, etc., 2007

[63] S. Redaelli, *Stabilization of Nanometre-Size Particle Beams in the Final Focus System of the Compact LInear Collider (CLIC)*, PhD thesis, Lausanne Inst. Phys. Hautes Energies, 2003.

[64] H. Braun et al, *CLIC 2008 Parameters*, CLIC-Note-764, 2008 http://cdsweb.cern.ch/record/1132079/files/CERN-OPEN-2008-021.pdf

[65] R. Tomas, private communication, 2010

[66] R. Brinkmann et al, *TESLA: The Superconducting Electron Positron Linear Collider with an Integrated X-Ray Laser Laboratory. Technical Design Report. Part. 2: The Accelerator*. DESY-2001-011, 2001

[67] F. Zimmermann, *Beam Dynamics Challenges for Future Circular Colliders*, Proc. 9th European Particle Accelerator Conference (EPAC 2004), Lucerne, Switzerland, 5-9 July 2004

[68] P. Schmüser, *Basic Principles of RF Superconductivity and Superconducting Cavities*, SRF2003, 2003

[69] F. Zimmermann et al, *The Large Hadron-Electron Collider (LHeC) at the LHC*, Proc. PAC'09 Vancouver, 4-8 May 2009, 2009

[70] LHeC web site *https://www.lhec.org.uk*

[71] D. Schulte, F. Zimmermann, *QCD Explorer Based on LHC and CLIC-1*, Proc. 9th European Particle Accelerator Conference (EPAC 2004), Lucerne, Switzerland, 5-9 July 2004